





Cite this: *Phys. Chem. Chem. Phys.*,  
2025, 27, 1402

# Ab initio electronic structures and total internal partition sums of FeH<sup>+/2+</sup>†

Isuru R. Ariyaratna,  \* Jeffery A. Leiding, Amanda J. Neukirch  and Mark C. Zammit

In the present work, we studied 27 FeH<sup>+</sup> and 6 FeH<sup>2+</sup> electronic states using multireference configuration interaction (MRCI), Davidson-corrected MRCI (MRCI+Q), and coupled cluster singles doubles and perturbative triples [CCSD(T)] wavefunction theory (WFT) calculations conjoined with large quadruple- $\zeta$  and quintuple- $\zeta$  quality correlation consistent basis sets. We report their potential energy curves (PEC), energy related properties, spectroscopic parameters, and spin-orbit couplings. Dipole moment curves (DMC) and transition dipole moment curves (TDMC) of several low-lying electronic states of FeH<sup>+</sup> and FeH<sup>2+</sup> are also introduced. The ground state of FeH<sup>+</sup> is a single-reference X<sup>5</sup> $\Delta$  (6 $\sigma^2$ 7 $\sigma^1$ 3 $\pi^2$ 1 $\delta^3$ ) with an adiabatic  $D_0$  of  $\sim 52$  kcal mol<sup>-1</sup>, which is in agreement with the experimental value. The states with the largest adiabatic binding energies of FeH<sup>2+</sup> (<sup>4</sup> $\Pi$  and <sup>4</sup> $\Delta$ ) are multireference in nature with an approximate  $D_0$  of 22 kcal mol<sup>-1</sup>. We used CCSD(T)  $\mu$  of the FeH<sup>+</sup>(X<sup>5</sup> $\Delta$ ) to assess the density functional theory (DFT) errors associated with a series of functionals that span multiple rungs of Jacob's ladder of density functional approximation (DFA) and observed a general trend of improving  $\mu$  when moving to more expensive functionals at the higher rungs. We expect weak spectral bands to be produced from the low-lying electronic states of FeH<sup>2+</sup> and FeH<sup>+</sup> due to their lower transition  $\mu$  values. Lastly, we present results for the total internal partition function sums (TIPS) of FeH<sup>+</sup> and FeH<sup>2+</sup>, which have not been presented in the literature before.

Received 22nd August 2024,  
Accepted 3rd December 2024

DOI: 10.1039/d4cp03296a

rsc.li/pccp

## 1. Introduction

The diatomic iron hydride cation FeH<sup>+</sup> is predicted to be abundant in cool stellar atmospheres.<sup>1</sup> However, due to the deficiency of available laboratory spectroscopic data on FeH<sup>+</sup>, its astronomical presence is yet to be observed. Aiming to guide and motivate experimental analysis of FeH<sup>+</sup> so far, a series of theoretical and computational attempts have been made specifically for gaining insight into its spectral features.

The first observation of the FeH<sup>+</sup> goes back to the 1979 Mysov *et al.*'s mass spectroscopic fragment analysis study of (CH<sub>3</sub>C<sub>5</sub>H<sub>4</sub>)<sub>2</sub>Fe.<sup>2</sup> Five years later, Halle, Klein, and Beauchamp analyzed the thresholds of the Fe<sup>+</sup> + H<sub>2</sub> and Fe<sup>+</sup> + D<sub>2</sub> reactions using ion beam apparatus and obtained the  $D_0$  of FeH<sup>+</sup> (59  $\pm$  5 kcal mol<sup>-1</sup>).<sup>3</sup> In 1986, Schilling *et al.*<sup>4</sup> performed an *ab initio*

generalized valence bond plus configuration interaction study and assigned a <sup>5</sup> $\Delta$  ground state with a 47.0 kcal mol<sup>-1</sup>  $D_0$  to FeH<sup>+</sup> which is significantly lower than the experimental value obtained by Halle *et al.*<sup>3</sup> In the same year, Elkind and Armentrout carried out a guided ion beam mass spectrometric study and reported a  $D_0$  of 48.9  $\pm$  1.4 kcal mol<sup>-1</sup> for FeH<sup>+</sup><sup>5</sup> which is in agreement with Schilling *et al.*'s work.<sup>4</sup> Furthermore, they intuitively projected low-lying <sup>5</sup> $\Pi$  and <sup>5</sup> $\Sigma^+$  electronic states for FeH<sup>+</sup> with  $\sigma^3\pi^3\delta^2$  and  $\sigma^4\pi^2\delta^2$  electronic configurations, respectively. In 1987 Schilling *et al.*, conducted another theoretical study and provided theoretical evidence for the existence of the <sup>5</sup> $\Pi$  and <sup>5</sup> $\Sigma^+$  excited states for FeH<sup>+</sup> lying 2.1 and 10.0 kcal mol<sup>-1</sup> above.<sup>6</sup> In the same year, Lars *et al.*, carried out modified coupled-pair functional (MCPF) calculations to predict  $r_e$  (1.603 Å),  $\omega_e$  (1805 cm<sup>-1</sup>), and  $\mu$  (2.41 D) values of FeH<sup>+</sup>(<sup>5</sup> $\Delta$ ).<sup>7</sup> They further estimated the  $D_0$  of FeH<sup>+</sup> to be 52.3 kcal mol<sup>-1</sup>, which is 2 kcal mol<sup>-1</sup> greater than the upper bound of the  $D_0$  reported by Elkind and Armentrout.<sup>5</sup> Two years later, Sodupe, Lluh, and Oliva studied the PEC originating from the Fe<sup>+</sup>(<sup>6</sup>D) + H(<sup>2</sup>S) fragments using the restricted open Hartree-Fock (ROHF) and configuration interaction levels.<sup>8</sup> In line with the previous reports, their ROHF calculations predicted a <sup>5</sup> $\Delta$  ground state for FeH<sup>+</sup>. However, they found that the inclusion of the electron correlation leads to a <sup>5</sup> $\Pi$  ground state for FeH<sup>+</sup>. According to their potential energy profile, all the septet-spin electronic

*Physics and Chemistry of Materials (T-1), Los Alamos National Laboratory, Los Alamos, NM 87545, USA. E-mail: isuru@lanl.gov*

† Electronic supplementary information (ESI) available: Fig. S1 illustrates the molecular orbitals of FeH<sup>+</sup>; Fig. S2 illustrates the  $\mu$  of FeH<sup>+</sup>(<sup>1</sup> $\Sigma^+$ ) under various functionals of DFT; Table S1 lists the total DFT  $\mu$  of FeH<sup>+</sup>(<sup>1</sup> $\Sigma^+$ ) and % DFT errors compared to CCSD(T)  $\mu$ ; Tables S2 and S3 list the TIPS fit coefficients of FeH<sup>+</sup> and FeH<sup>2+</sup>; Table S4 lists the absolute energies of the electronic states of the FeH<sup>+</sup>; Table S5 lists the absolute energies and the spectroscopic parameters of FeH<sup>+</sup> at CAS(8,7); Table S6 lists the absolute energies of the electronic states of the FeH<sup>2+</sup>. See DOI: <https://doi.org/10.1039/d4cp03296a>



states originating from the ground state fragments are repulsive in nature. This observation was further corroborated by a study reported by Langhoff and Bauschlicher in 1991.<sup>9</sup> Specifically, Langhoff and Bauschlicher carried out a theoretical spectroscopic study for  $\text{FeH}^+$  utilizing CASSCF (complete active space self-consistent field), MRCI, and MCPF levels of theory.<sup>9</sup> The CASSCF order of the states that they observed was  $X^5\Delta$ ,  $A^5\Pi$ ,  $B^5\Sigma^+$ ,  $a^3\Sigma^-$ ,  $b^3\Phi$ ,  $c^3\Pi$ , and  $d^3\Delta$ . They reported the MRCI  $X^5\Delta \rightarrow A^5\Pi$  and  $X^5\Delta \rightarrow a^3\Sigma^-$  transition energies of  $\text{FeH}^+$  to be 669 and 10 277  $\text{cm}^{-1}$ , respectively. Moreover, their study predicted a  $D_0$  of 50.2  $\text{kcal mol}^{-1}$  for  $\text{FeH}^+$ . In 2019, Cheng and DeYonker analyzed the low-lying  $X^5\Delta$ ,  $A^5\Pi$ ,  $B^5\Sigma^+$ ,  $a^3\Sigma^-$ ,  $b^3\Phi$ ,  $c^3\Pi$ , and  $d^3\Delta$  states of  $\text{FeH}^+$  using MRCI and coupled cluster levels of theories.<sup>10</sup> This is clearly the most complete work reported for  $\text{FeH}^+$  so far. Their work utilized a highly accurate focal point approach to calculate the  $X^5\Delta \rightarrow A^5\Pi$  (600  $\text{cm}^{-1}$ ) and  $X^5\Delta \rightarrow a^3\Sigma^-$  (10 081  $\text{cm}^{-1}$ ) transition energies and ionization energy (IE) of  $\text{FeH}$  (7.4851 eV).<sup>10</sup> Furthermore, this work reported a series of spectroscopic constants for the aforementioned states. The most recent study related to  $\text{FeH}^+$  was reported in 2022 by the Beyer group.<sup>11</sup> Here they performed infrared multiple photon dissociation (IRMPD) spectroscopic analysis for  $\text{Ar}_2\text{FeH}^+$  aiming to guide future experimental spectroscopic studies of  $\text{FeH}^+$ .

To the best of our knowledge, experimental spectroscopic analysis has not been conducted for  $\text{FeH}^{2+}$  before. We were only able to locate one WFT based study for this system which was reported by Wilson, Marsden, Nagy-Felsobuki in 2003.<sup>12</sup> This study predicted a  $^4\Delta$  ground state for  $\text{FeH}^{2+}$  with  $D_e$  (dissociation energy),  $r_e$ , and  $\omega_e$  values of 21.68  $\text{kcal mol}^{-1}$ , 1.998 Å, and 830  $\text{cm}^{-1}$ , respectively under the MRCI+Q level of theory.

In the present work we have utilized *ab initio* MRCI<sup>13–15</sup> method and MRCI+Q<sup>16</sup> correction to analyze the  $\text{Fe}^+ + \text{H}$  and  $\text{Fe}^{2+} + \text{H}$  reactions and to investigate the ground and electronically excited states of  $\text{FeH}^+$  and  $\text{FeH}^{2+}$  species. The implemented MRCI is indeed capable of providing accurate results for both multireference and single-reference electronic states of highly correlated transition metal-based species such as  $\text{FeH}^+$  and  $\text{FeH}^{2+}$ . Especially, this level of theory is ideal for efficiently producing full PEC for a large number of electronic states of diatomic molecules. On the other hand, the approximate quadruple substitution effect provided by MRCI+Q<sup>16</sup> is often being used to gain more accurate results and reach experimental observations.

Here, we report 27 and 6 MRCI PEC of  $\text{FeH}^+$  and  $\text{FeH}^{2+}$ , respectively. Under MRCI,<sup>13–15</sup> MRCI+Q,<sup>16</sup> and CCSD(T)<sup>17</sup> levels, their equilibrium electronic configurations, various energy related properties, and a set of spectroscopic parameters are reported. At the MRCI level, the spin-orbit effects of  $\text{FeH}^+$  and  $\text{FeH}^{2+}$  were also evaluated. Furthermore, MRCI DMC and TDMC corresponding to several low-lying electronic states of  $\text{FeH}^+$  and  $\text{FeH}^{2+}$  are introduced. The CCSD(T)  $\mu$  analyses were also performed for low-lying single-reference electronic states. The  $\mu$  of the single-reference  $\text{FeH}^+(X^5\Delta)$  were also analyzed with 17 functionals that span multiple families of DFA<sup>18</sup> [i.e., semi-local generalized gradient approximation (GGA), meta-GGA (MGGA), global GGA hybrid, MGGA

hybrid, range-separated hybrid (RSH), double hybrid (DH)]. Finally, we used the MRCI PEC of  $\text{FeH}^+$  and  $\text{FeH}^{2+}$  to calculate their TIPS values. We believe that the findings of this work will serve as a guide for future theoretical studies of similar transition metal-based diatomic species and for experimental analysis and identification of  $\text{FeH}^+$  and  $\text{FeH}^{2+}$  in the interstellar space.

## II. Computational details

The internally contracted MRCI ( $\equiv \text{MRCISD}$ )<sup>13–15</sup> and CCSD(T)<sup>17</sup> calculations were performed using the MOLPRO 2023.2<sup>19–21</sup> code. First, full MRCI PEC of  $\text{FeH}^+$  and  $\text{FeH}^{2+}$  were produced using the quadruple- $\zeta$  quality correlation consistent aug-cc-pVQZ basis set for both atoms.<sup>22,23</sup> Specifically, the PEC arising from  $\text{Fe}^+(^6\text{D}) + \text{H}(^2\text{S})$ ,  $\text{Fe}^+(^4\text{F}) + \text{H}(^2\text{S})$ ,  $\text{Fe}^+(^4\text{D}) + \text{H}(^2\text{S})$ ,  $\text{Fe}^+(^4\text{P}) + \text{H}(^2\text{S})$ , and  $\text{Fe}^+(^2\text{G}) + \text{H}(^2\text{S})$  were considered to study the low-lying electronic states of  $\text{FeH}^+$ . On the other hand, the PEC of  $\text{Fe}^{2+}(^5\text{D}) + \text{H}(^2\text{S})$  were analyzed to investigate the electronic states of  $\text{FeH}^{2+}$ . CASSCF<sup>24–27</sup> wavefunctions were provided for all MRCI calculations. The CASSCF wave function of  $\text{FeH}^+$  were produced by allocating 8 electrons in 12 orbitals [CAS(8,12)]. At the dissociation limit, the active orbitals are the pure atomic orbitals of the five 3d, five 4d, and 4s of Fe and the 1s of H. The same set of orbitals were provided to build CASSCF active space of  $\text{FeH}^{2+}$  with 7 active electrons [CAS(7,12)]. Under the utilized  $C_{2v}$  Abelian point-group, the active orbitals are  $6a_1$  ( $3d_{z^2}$ ,  $3d_{x^2-y^2}$ ,  $4d_{z^2}$ ,  $4d_{x^2-y^2}$ , and 4s of Fe and 1s of H),  $2b_1$  ( $3d_{xz}$  and  $4d_{xz}$  of Fe),  $2b_2$  ( $3d_{yz}$  and  $4d_{yz}$  of Fe), and  $2a_2$  ( $3d_{xy}$  and  $4d_{xy}$  of Fe). At the MRCI level, the single and double electron substitutions from active to virtual orbitals were allowed. The *ad hoc* Davidson correction (MRCI+Q) was applied as a size-extensivity correction.<sup>16</sup> The MRCI and MRCI+Q potential wells of  $\text{FeH}^+$  and  $\text{FeH}^{2+}$  were utilized to solve the rovibrational Schrödinger equation numerically and obtain their harmonic vibrational frequencies ( $\omega_e$ ), anharmonicities ( $\omega_e x_e$ ), equilibrium rotational constants ( $B_e$ ), anharmonic correction to the rotational constants ( $\alpha_e$ ), and centrifugal distortion constants ( $\bar{D}_e$ ). At the MRCI level, DMC and TDMC of several low-lying electronic states of  $\text{FeH}^+$  and  $\text{FeH}^{2+}$  were also produced using the same basis set and active spaces. To evaluate the relativistic effects on the energetics and the spectroscopic constants, potential energy scans were performed at the MRCI and MRCI+Q levels for the 7 and 6 lowest electronic states of  $\text{FeH}^+$  and  $\text{FeH}^{2+}$ , respectively. For these calculations, the aug-cc-pVQZ-DK basis set and the second-order Douglas-Kroll-Hess Hamiltonian were used. Hereafter these calculations are denoted by AQZ-DK-MRCI and AQZ-DK-MRCI+Q. At the AQZ-DK-MRCI level, spin-orbit coupling effects were evaluated by implementing the Breit-Pauli Hamiltonian (more information on the spin-orbit analysis is given in the Discussion section).

The CCSD(T) calculations were performed for a few single-reference electronic states of  $\text{FeH}^+$  and  $\text{FeH}^{2+}$  utilizing the restricted Hartree-Fock (RHF) wave functions. For CCSD(T) calculations, 3 types of correlation consistent basis sets were used: (1) aug-cc-pVQZ/<sub>Fe,H</sub>, (2) aug-cc-pV5Z/<sub>Fe,H</sub>, (3) aug-cc-pwCV5Z/<sub>Fe</sub> aug-cc-pV5Z/<sub>H</sub>.<sup>22,23</sup> Hereafter these CCSD(T) calculations are denoted by AQZ-CCSD(T), A5Z-CCSD(T), and c-A5Z-CCSD(T),



respectively. Note that the  $3s^2$  and  $3p^6$  core electrons of Fe were correlated at the c-A5Z-CCSD(T).<sup>22</sup> The CCSD(T) potential energy scans performed around the equilibrium distance region of the electronic states were utilized to calculate their  $D_e$ ,  $r_e$ ,  $\omega_e$ ,  $\omega_e x_e$ ,  $B_e$ ,  $\alpha_e$ , and  $\bar{D}_e$  values. Combined with the findings from a previous work of ours, the IE of FeH was calculated at the CCSD(T) level.<sup>28</sup> The CCSD(T)  $\mu$  values of the low-lying single-reference electronic states of  $\text{FeH}^+$  and  $\text{FeH}^{2+}$  were also computed with the finite-field method. For these CCSD(T)  $\mu$  calculations, a field ( $f$ ) of 0.01 a.u. was applied to the positive and negative directions of  $\text{FeH}^+$  and  $\text{FeH}^{2+}$  and the calculated  $E(f)$  and  $E(-f)$  energies were provided for the  $\mu = [E(f) - E(-f)]/2f$  equation. The  $\mu$  of the single-reference  $\text{FeH}^+(\text{X}^5\Delta)$  was also calculated with DFT using a series of functionals belongs to different families of DFA; semi-local generalized gradient approximation (GGA: BP86,<sup>29,30</sup> BLYP,<sup>31,32</sup> PBE<sup>33</sup>), meta-GGA (MGGA: TPSS,<sup>34</sup> MN15-L<sup>35</sup>), global GGA hybrid (B3LYP,<sup>36–38</sup> B3P86,<sup>29,36</sup> B3PW91,<sup>36,39</sup> PBE0<sup>40</sup>), MGGA hybrid (TPSSH,<sup>34</sup> M06-2X,<sup>41</sup> MN15<sup>42</sup>), range-separated hybrid (RSH: LRC- $\omega$ PBE,<sup>43</sup> CAM-B3LYP,<sup>44</sup>  $\omega$ B97X<sup>45</sup>), and double hybrid (DH: PBE0-DH,<sup>46</sup> DSDPBEP86<sup>47,48</sup>). The DFT  $\mu$  values were calculated at the previously reported DFT  $r_e$  values of  $\text{FeH}^+(\text{X}^5\Delta)$  combined with the aug-cc-pVQZ basis set.<sup>28</sup> In all cases, the default origins (center of the mass) were used for the dipole moment calculations. For DFT calculations, Gaussian 16<sup>49</sup> software was used.

The TIPS,  $Q$ , of a species can be evaluated *via*

$$Q = \sum_j g_j \exp\left(-\frac{E_{j,0}}{k_B T}\right),$$

where  $g_j$  is the degeneracy or statistical weight (including the nuclear spin) of level  $j$ ,  $k_B$  is the Boltzmann constant,  $T$  is the temperature, and  $E_{j,0}$  is the excitation energy of level  $j$  from the ground state. For the evaluation of the  $\text{FeH}^+$  and  $\text{FeH}^{2+}$  TIPS, rovibrational energy levels were calculated by solving the rovibrational Schrödinger equation,<sup>50</sup> where all bound rovibrational levels<sup>50</sup> within the 27 electronic states of  $\text{FeH}^+$  and 6 electronic states of  $\text{FeH}^{2+}$  were included in the sum.

### III. Results and discussion

#### III.A. $\text{FeH}^+$

The implementation of large active spaces that include additional diffuse type d-functions, rather than traditional valence orbitals-based spaces has been tested to provide more accurate energetics and electronic structures for group 8 transition metal-based diatomic systems (*i.e.*, FeH,  $\text{FeO}^{2+}$ ,  $\text{RuO}^{2+}$ ).<sup>28,51,52</sup> Similarly, in the current study we have utilized large active spaces that are made of the five 3d, five 4d, and the 4s, atomic orbitals of Fe and the 1s atomic orbital of H for all of our multireference calculations. Using this active space, first we studied several CASSCF PEC of  $\text{FeH}^+$  that are originating from various asymptotes of  $\text{Fe}^+$  and H.

The ground state of  $\text{Fe}^+$  is a  $^6\text{D}$  with  $3d^6 4s^1$  valence electron configuration.<sup>53</sup> The transfer of the  $4s^1$  electron to 3d orbitals produces its first excited state  $^4\text{F}$  (at  $\sim 5.35$ – $8.91$  kcal mol<sup>-1</sup>).<sup>53</sup> The second excited state of  $\text{Fe}^+$  ( $^4\text{D}$ ) has an electron arrangement

similar to the ground state, but with a lower spin due to the electron coupling ( $^4\text{D}$ ; at 22.75–25.29 kcal mol<sup>-1</sup>).<sup>53</sup> The next state of  $\text{Fe}^+$  is a  $^4\text{P}$  with  $3d^7$  configuration (at 38.53–39.76 kcal mol<sup>-1</sup>).<sup>53</sup> The fourth excited state of  $\text{Fe}^+$  is indeed the first doublet-spin electronic state of  $\text{Fe}^+$  ( $^2\text{G}$ ;  $3d^7$ ) lying at 45.30–46.80 kcal mol<sup>-1</sup>.<sup>53</sup> The interactions of all these electronic states of  $\text{Fe}^+$  with the  $\text{H}(^2\text{S})$  ground state were selected to investigate the low-lying electronic states of  $\text{FeH}^+$ . The reactions between  $\text{Fe}^+(^6\text{D}) + \text{H}(^2\text{S})$ ,  $\text{Fe}^+(^4\text{F}) + \text{H}(^2\text{S})$ ,  $\text{Fe}^+(^4\text{D}) + \text{H}(^2\text{S})$ ,  $\text{Fe}^+(^4\text{P}) + \text{H}(^2\text{S})$ , and  $\text{Fe}^+(^2\text{G}) + \text{H}(^2\text{S})$  give rise to  $^7\Sigma^+$ ,  $\Pi$ ,  $\Delta$ ,  $^5\Sigma^-$ ,  $\Pi$ ,  $\Delta$ ,  $\Phi$ ,  $^5\Sigma^+$ ,  $\Pi$ ,  $\Delta$ ,  $^5\Sigma^-$ ,  $\Pi$ , and  $^3\Sigma^+$ ,  $\Pi$ ,  $\Delta$ ,  $\Phi$ ,  $\Gamma$  states.<sup>54,55</sup> We used the CASSCF PEC of the aforementioned asymptotes to identify the lowest energy electronic states of  $\text{FeH}^+$ ; specifically its most stable 27 states were studied under the MRCI level of theory. Our calculated MRCI potential energy profile is given in the Fig. 1. Since we did not consider the interaction of excited states of H with the low-lying electronic states of  $\text{Fe}^+$  (due to the excitation energy of H atom being significantly higher), the energies of the fragments at the right side of the potential energy profile correspond to the excitation energies of  $\text{Fe}^+$ . As expected, at the dissociation limit, the first 4 excitation energies of  $\text{Fe}^+$  at the MRCI level are  $\sim 4$ , 22, 37, and 46 kcal mol<sup>-1</sup>, which are in reasonable agreement with the experimental values.<sup>53</sup>

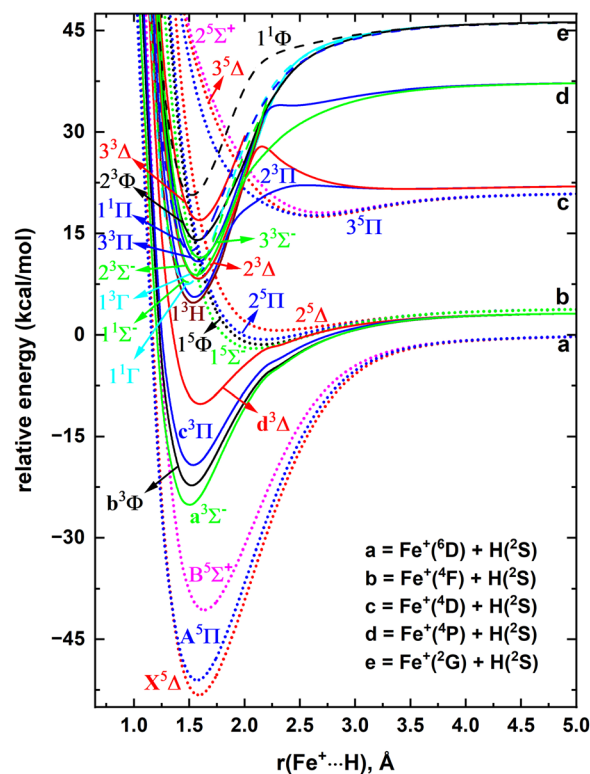


Fig. 1 MRCI/aug-cc-pVQZ PEC of  $\text{FeH}^+$  as a function of  $\text{Fe}^+ \cdots \text{H}$  distance [ $r(\text{Fe}^+ \cdots \text{H})$ , Å]. The relative energies are with respect to the total energy of  $\text{Fe}^+(^6\text{D}) \cdots \text{H}(^2\text{S})$  when they are at 200 Å separation, which is set to 0 kcal mol<sup>-1</sup>. The dotted, solid, and dashed PEC correspond to the quintet, triplet, and singlet spins, respectively. The  $\Delta$ ,  $\Pi$ ,  $\Sigma^+$ ,  $\Sigma^-$ ,  $\Phi$ ,  $\Gamma$ , and H states are shown in red, blue, pink, green, black, cyan, and brown, respectively.



All 3 quintet-spin electronic states originating from the  $\text{Fe}^+(\text{6D}) + \text{H}(\text{2S})$  are strongly attractive and become the first 3 electronic states of  $\text{FeH}^+$  (*i.e.*,  $\text{X}^5\Delta$ ,  $\text{A}^5\Pi$ , and  $\text{B}^5\Sigma^+$ ). Note that within the studied energy range, the septet-spin PEC of the same asymptote are repulsive and do not form minima, and hence are not illustrated in Fig. 1. This is consistent with the previous analysis of the PEC of  $\text{FeH}^+$ .<sup>8,9,56</sup> The next 4 states of  $\text{FeH}^+$  are triplet in spin (*i.e.*,  $\text{a}^3\Sigma^-$ ,  $\text{b}^3\Phi$ ,  $\text{c}^3\Pi$ ,  $\text{d}^3\Delta$ ) and dissociate to the second lowest energy asymptote  $\text{Fe}^+(\text{4F}) + \text{H}(\text{2S})$ . The quintet-spin states of the same fragments are mildly attractive and form shallow minima around 2–2.3 Å. Interestingly, the ordering of these quintet-spin states (*i.e.*,  $1^5\Sigma^-$ ,  $1^5\Phi$ ,  $2^5\Pi$ ,  $2^5\Delta$ ) of  $\text{Fe}^+(\text{4F}) + \text{H}(\text{2S})$  is the same as the ordering of its triplet-spin states. Beyond this point, the electronic spectrum of  $\text{FeH}^+$  is quite complicated with a series of closely arranged electronic states dissociating to  $\text{Fe}^+(\text{4D}) + \text{H}(\text{2S})$ ,  $\text{Fe}^+(\text{4P}) + \text{H}(\text{2S})$ ,  $\text{Fe}^+(\text{2G}) + \text{H}(\text{2S})$ , and more high energy fragments (Fig. 1).

The equilibrium electronic configurations of the studied 27 electronic states of  $\text{FeH}^+$  are reported in the Table 1. The contours of the occupying molecular orbitals are given in ESI† Fig. S1. Notice that the first 3 electronic states of  $\text{FeH}^+$  are dominantly single-reference in nature. The  $\text{X}^5\Delta$  has the  $6\sigma^2 7\sigma^1 3\pi^2 1\delta^3$  configuration and the attachment of an electron to its  $7\sigma$  orbital produces the dominant electronic configuration of the ground state of  $\text{FeH}$  ( $\text{X}^4\Delta$ ).<sup>28</sup> The first excited state of  $\text{FeH}^+$  is formed by transferring an electron from the doubly occupied  $1\delta$  orbital to a  $3\pi$  orbital ( $6\sigma^2 7\sigma^1 3\pi^3 1\delta^2$ ). Similar to the ground state, placing an electron in the singly occupied  $7\sigma$  of  $\text{FeH}^+(\text{A}^5\Pi)$  gives rise to the first excited state of  $\text{FeH}$  ( $\text{A}^4\Pi$ ).<sup>28</sup> On the other hand, the electronic structures of  $\text{B}^5\Sigma^+$  of  $\text{FeH}^+$  and  $\text{c}^6\Sigma^+$  of  $\text{FeH}$  (fifth excited state of  $\text{FeH}$ ) are closely related except for the additional electron occupying in the  $8\sigma$  of  $\text{FeH}(\text{c}^6\Sigma^+)$ .<sup>28</sup> The third excited state of  $\text{FeH}^+$  (*i.e.*,  $\text{a}^3\Sigma^-$ ) has a major configuration of  $6\sigma^2 3\pi^4 1\delta^2$  but bears a small contribution of  $6\sigma^2 3\pi^2 1\delta^4$  as well. The next 3 states are chiefly multi-reference in nature (*i.e.*,  $\text{b}^3\Phi$ ,  $\text{c}^3\Pi$ ,  $\text{d}^3\Delta$ ). Similarly, all other studied states are multi-reference except for the slightly bound  $1^5\Sigma^-$  and  $2^5\Delta$  states (Table 1 and Fig. 1).

The predominantly single-reference  $\text{X}^5\Delta$ ,  $\text{A}^5\Pi$ , and  $\text{B}^5\Sigma^+$  states of  $\text{FeH}^+$  provide us with the opportunity of performing single-reference CCSD(T) calculations for them. The CCSD(T) calculations were performed on top of the RHF wave functions that were produced for their dominant electronic configurations listed in the Table 1. The results of the CCSD(T) calculations carried out with AQZ and A5Z basis sets are listed in the Table 2 along with the AQZ-MRCI and AQZ-MRCI+Q values of  $\text{FeH}^+$ . Note that the larger A5Z basis set was only utilized with the CCSD(T) method since CCSD(T) level is relatively less expensive compared to the MRCI level. Furthermore, due to the less demanding nature of CCSD(T) (compared to MRCI), we evaluated the core electron correlation effects on various properties of  $\text{FeH}^+$  by unfreezing the  $3s^2$  and  $3p^6$  core electrons of  $\text{Fe}^+$  with the application of proper aug-cc-pwCV5Z basis set of Fe and the results are reported in the Table 2.

The  $\text{FeH}^+(\text{X}^5\Delta)$  is  $\sim 8$  kcal mol<sup>−1</sup> more stable than  $\text{FeH}(\text{X}^4\Delta)$  [*i.e.*, the adiabatic  $D_e$  of  $\text{FeH}(\text{X}^4\Delta)$  at c-A5Z-CCSD(T) level is

**Table 1** Dominant electronic configurations of the 27 electronic states of  $\text{FeH}^+$  at their corresponding equilibrium distances

State <sup>a</sup>	Coefficient <sup>b</sup>	Configuration <sup>c</sup>
$\text{X}^5\Delta$ ( $\text{A}_1$ )	0.97	$6\sigma^2 7\sigma 3\pi_x 3\pi_y (1\delta_{x^2-y^2})^2 1\delta_{xy}$
$\text{A}^5\Pi$ ( $\text{B}_1$ )	0.97	$6\sigma^2 7\sigma 3\pi_x^2 3\pi_y (1\delta_{x^2-y^2}) 1\delta_{xy}$
$\text{B}^5\Sigma^+$	0.97	$6\sigma^2 7\sigma^2 3\pi_x 3\pi_y (1\delta_{x^2-y^2}) 1\delta_{xy}$
$\text{a}^3\Sigma^-$	0.87	$6\sigma^2 3\pi_x^2 3\pi_y^2 (1\delta_{x^2-y^2}) 1\delta_{xy}$
	−0.31	$6\sigma^2 3\pi_x 3\pi_y (1\delta_{x^2-y^2})^2 1\delta_{xy}^2$
$\text{b}^3\Phi$ ( $\text{B}_1$ )	0.65	$6\sigma^2 3\pi_x 3\pi_y^2 (1\delta_{x^2-y^2}) 1\delta_{xy}^2$
	0.65	$6\sigma^2 3\pi_x^2 3\pi_y (1\delta_{x^2-y^2})^2 1\delta_{xy}^2$
$\text{c}^3\Pi$ ( $\text{B}_1$ )	−0.52	$6\sigma^2 3\pi_x 3\pi_y^2 (1\delta_{x^2-y^2}) 1\delta_{xy}$
	0.52	$6\sigma^2 3\pi_x^2 3\pi_y (1\delta_{x^2-y^2})^2 1\delta_{xy}$
	−0.49	$6\sigma^2 7\sigma 3\pi_x^2 3\pi_y (1\delta_{x^2-y^2}) 1\delta_{xy}$
$\text{d}^3\Delta$ ( $\text{A}_1$ )	0.77	$6\sigma^2 7\sigma 3\pi_x 3\pi_y (1\delta_{x^2-y^2})^2 1\delta_{xy}$
	−0.34	$6\sigma^2 7\sigma 3\pi_x^2 3\pi_y (1\delta_{x^2-y^2})^2 1\delta_{xy}$
	−0.34	$6\sigma^2 7\sigma 3\pi_x^2 3\pi_y^2 (1\delta_{x^2-y^2})^2 1\delta_{xy}$
$1^5\Sigma^-$	0.90	$6\sigma^2 7\sigma 3\pi_x^2 3\pi_y^2 (1\delta_{x^2-y^2}) 1\delta_{xy}$
	0.33	$6\sigma^2 7\sigma 3\pi_x 3\pi_y (1\delta_{x^2-y^2})^2 1\delta_{xy}^2$
$1^5\Phi$ ( $\text{B}_1$ )	−0.68	$6\sigma^2 7\sigma 3\pi_x 3\pi_y^2 (1\delta_{x^2-y^2}) 1\delta_{xy}^2$
	0.68	$6\sigma^2 7\sigma 3\pi_x^2 3\pi_y (1\delta_{x^2-y^2})^2 1\delta_{xy}^2$
$2^5\Pi$ ( $\text{B}_1$ )	0.50	$6\sigma^2 7\sigma 3\pi_x 3\pi_y^2 (1\delta_{x^2-y^2}) 1\delta_{xy}^2$
	0.50	$6\sigma^2 7\sigma 3\pi_x^2 3\pi_y (1\delta_{x^2-y^2})^2 1\delta_{xy}^2$
	0.64	$6\sigma^2 7\sigma^2 3\pi_x^2 3\pi_y (1\delta_{x^2-y^2}) 1\delta_{xy}$
$2^5\Delta$ ( $\text{A}_1$ )	0.93	$6\sigma^2 7\sigma^2 3\pi_x 3\pi_y (1\delta_{x^2-y^2})^2 1\delta_{xy}$
$1^3\text{H}$ ( $\text{B}_1$ )	0.48	$6\sigma^2 7\sigma 3\pi_x^2 3\pi_y (1\delta_{x^2-y^2}) 1\delta_{xy}$
	−0.48	$6\sigma^2 7\sigma 3\pi_x 3\pi_y^2 (1\delta_{x^2-y^2})^2$
	−0.48	$6\sigma^2 7\sigma 3\pi_x 3\pi_y^2 1\delta_{xy}^2$
	−0.48	$6\sigma^2 7\sigma 3\pi_x^2 3\pi_y (1\delta_{x^2-y^2}) 1\delta_{xy}$
$2^3\Pi$ ( $\text{B}_1$ )	0.53	$6\sigma^2 7\sigma 3\pi_x^2 3\pi_y (1\delta_{x^2-y^2}) 1\delta_{xy}$
	−0.42	$6\sigma^2 7\sigma 3\pi_x^2 3\pi_y (1\delta_{x^2-y^2}) 1\delta_{xy}$
	0.40	$6\sigma^2 7\sigma 3\pi_x 3\pi_y^2 (1\delta_{x^2-y^2})^2$
	0.40	$6\sigma^2 7\sigma 3\pi_x 3\pi_y^2 1\delta_{xy}^2$
$1^1\Gamma$ ( $\text{A}_1$ )	−0.67	$6\sigma^2 3\pi_x^2 3\pi_y^2 (1\delta_{x^2-y^2})^2$
	0.67	$6\sigma^2 3\pi_x^2 3\pi_y^2 1\delta_{xy}$
$1^1\Sigma^-$	0.57	$6\sigma^2 3\pi_x^2 3\pi_y^2 (1\delta_{x^2-y^2})^2$
	0.57	$6\sigma^2 3\pi_x^2 3\pi_y^2 1\delta_{xy}$
$1^3\Gamma$ ( $\text{A}_1$ )	0.46	$6\sigma^2 7\sigma 3\pi_y^2 (1\delta_{x^2-y^2}) 1\delta_{xy}^2$
	−0.46	$6\sigma^2 7\sigma 3\pi_x^2 (1\delta_{x^2-y^2}) 1\delta_{xy}^2$
	−0.46	$6\sigma^2 7\sigma 3\pi_x 3\pi_y (1\delta_{x^2-y^2})^2 1\delta_{xy}$
	0.46	$6\sigma^2 7\sigma 3\pi_x 3\pi_y (1\delta_{x^2-y^2})^2 1\delta_{xy}$
$2^3\Delta$ ( $\text{A}_2$ )	0.68	$6\sigma^2 7\sigma 3\pi_x 3\pi_y (1\delta_{x^2-y^2}) 1\delta_{xy}^2$
	0.51	$6\sigma^2 7\sigma 3\pi_x^2 3\pi_y^2 1\delta_{xy}$
$2^3\Sigma^-$	−0.41	$6\sigma^2 7\sigma 3\pi_x^2 3\pi_y (1\delta_{x^2-y^2}) 1\delta_{xy}^2$
	0.41	$6\sigma^2 7\sigma 3\pi_x^2 3\pi_y (1\delta_{x^2-y^2}) 1\delta_{xy}^2$
	0.41	$6\sigma^2 7\sigma 3\pi_x^2 (1\delta_{x^2-y^2})^2 1\delta_{xy}$
	−0.41	$6\sigma^2 7\sigma 3\pi_y^2 (1\delta_{x^2-y^2})^2 1\delta_{xy}$
$3^3\Pi$ ( $\text{B}_1$ )	0.53	$6\sigma^2 7\sigma 3\pi_x^2 3\pi_y (1\delta_{x^2-y^2}) 1\delta_{xy}$
	0.53	$6\sigma^2 7\sigma 3\pi_x (1\delta_{x^2-y^2})^2 1\delta_{xy}^2$
	−0.31	$6\sigma^2 7\sigma 3\pi_x^2 3\pi_y (1\delta_{x^2-y^2}) 1\delta_{xy}$
	−0.31	$6\sigma^2 7\sigma 3\pi_x^2 3\pi_y (1\delta_{x^2-y^2}) 1\delta_{xy}$
$3^3\Sigma^-$	0.57	$6\sigma^2 3\pi_x 3\pi_y (1\delta_{x^2-y^2})^2 1\delta_{xy}^2$
	−0.40	$6\sigma^2 7\sigma^2 3\pi_x 3\pi_y 1\delta_{xy}^2$
	−0.40	$6\sigma^2 7\sigma^2 3\pi_x 3\pi_y (1\delta_{x^2-y^2})^2$
$1^1\Pi$ ( $\text{B}_1$ )	−0.43	$6\sigma^2 3\pi_x^2 3\pi_y (1\delta_{x^2-y^2})^2 1\delta_{xy}$
	0.43	$6\sigma^2 3\pi_x^2 3\pi_y (1\delta_{x^2-y^2})^2 1\delta_{xy}$
	0.43	$6\sigma^2 3\pi_x^2 3\pi_y^2 (1\delta_{x^2-y^2}) 1\delta_{xy}^2$
	−0.43	$6\sigma^2 3\pi_x 3\pi_y^2 (1\delta_{x^2-y^2}) 1\delta_{xy}^2$
$2^3\Phi$ ( $\text{B}_1$ )	0.41	$6\sigma^2 7\sigma 3\pi_x^2 3\pi_y (1\delta_{x^2-y^2}) 1\delta_{xy}$
	−0.41	$6\sigma^2 7\sigma 3\pi_x 3\pi_y^2 (1\delta_{x^2-y^2})^2$
	0.41	$6\sigma^2 7\sigma 3\pi_x 3\pi_y^2 1\delta_{xy}^2$
	−0.41	$6\sigma^2 7\sigma 3\pi_x^2 3\pi_y (1\delta_{x^2-y^2}) 1\delta_{xy}$
$3^3\Delta$ ( $\text{A}_1$ )	0.47	$6\sigma^2 7\sigma 3\pi_y^2 (1\delta_{x^2-y^2}) 1\delta_{xy}^2$
	0.47	$6\sigma^2 7\sigma 3\pi_x^2 (1\delta_{x^2-y^2}) 1\delta_{xy}^2$
	−0.39	$6\sigma^2 7\sigma^2 3\pi_x 3\pi_y (1\delta_{x^2-y^2}) 1\delta_{xy}$





Table 1 (continued)

State <sup>a</sup>	Coefficient <sup>b</sup>	Configuration <sup>c</sup>
3 <sup>5</sup> Δ (A <sub>1</sub> )	0.39	6σ <sup>2</sup> 7σ <sup>2</sup> 3π <sub>x</sub> 3π <sub>y</sub> (1δ <sub>x<sup>2</sup>-y<sup>2</sup></sub> )1δ <sub>xy</sub>
	0.70	6σ <sup>2</sup> 7σ <sup>2</sup> 8σ <sup>2</sup> 3π <sub>x</sub> 3π <sub>y</sub> (1δ <sub>x<sup>2</sup>-y<sup>2</sup></sub> ) <sup>2</sup> 1δ <sub>xy</sub>
	0.32	6σ <sup>2</sup> 7σ <sup>2</sup> 8σ <sup>2</sup> 3π <sub>x</sub> 3π <sub>y</sub> (1δ <sub>x<sup>2</sup>-y<sup>2</sup></sub> ) <sup>2</sup> 1δ <sub>xy</sub>
3 <sup>5</sup> Π (B <sub>1</sub> )	0.71	6σ <sup>2</sup> 7σ <sup>2</sup> 8σ <sup>2</sup> 3π <sub>x</sub> 3π <sub>y</sub> (1δ <sub>x<sup>2</sup>-y<sup>2</sup></sub> )1δ <sub>xy</sub>
	0.31	6σ <sup>2</sup> 7σ <sup>2</sup> 3π <sub>x</sub> 3π <sub>y</sub> (1δ <sub>x<sup>2</sup>-y<sup>2</sup></sub> )1δ <sub>xy</sub>
2 <sup>5</sup> Σ <sup>+</sup>	0.73	6σ <sup>2</sup> 7σ <sup>2</sup> 8σ <sup>2</sup> 3π <sub>x</sub> 3π <sub>y</sub> (1δ <sub>x<sup>2</sup>-y<sup>2</sup></sub> )1δ <sub>xy</sub>
	0.30	6σ <sup>2</sup> 7σ <sup>2</sup> 3π <sub>x</sub> 3π <sub>y</sub> (1δ <sub>x<sup>2</sup>-y<sup>2</sup></sub> )1δ <sub>xy</sub>
1 <sup>4</sup> Φ (B <sub>1</sub> )	0.36	6σ <sup>2</sup> 3π <sub>x</sub> <sup>2</sup> 3π <sub>y</sub> (1δ <sub>x<sup>2</sup>-y<sup>2</sup></sub> ) <sup>2</sup> 1δ <sub>xy</sub>
	−0.36	6σ <sup>2</sup> 3π <sub>x</sub> <sup>2</sup> 3π <sub>y</sub> (1δ <sub>x<sup>2</sup>-y<sup>2</sup></sub> ) <sup>2</sup> 1δ <sub>xy</sub>
	0.36	6σ <sup>2</sup> 3π <sub>x</sub> 3π <sub>y</sub> (1δ <sub>x<sup>2</sup>-y<sup>2</sup></sub> )1δ <sub>xy</sub> <sup>2</sup>
	−0.36	6σ <sup>2</sup> 3π <sub>x</sub> 3π <sub>y</sub> (1δ <sub>x<sup>2</sup>-y<sup>2</sup></sub> )1δ <sub>xy</sub> <sup>2</sup>

<sup>a</sup> The corresponding C<sub>2v</sub> symmetries of Δ, Π, Φ, Γ, and H are listed in parenthesis. <sup>b</sup> All the CI coefficients that are larger than 0.3 of corresponding natural orbital representations are listed. <sup>c</sup> β and α-spin electrons are specified with and without bars over the spatial orbital, respectively.

46.06 kcal mol<sup>−1</sup>].<sup>28</sup> The AQZ-MRCI level predicted a *D*<sub>e</sub> of 53.27 kcal mol<sup>−1</sup> for the FeH<sup>+</sup>(X<sup>5</sup>Δ). MRCI+Q increased the *D*<sub>e</sub> by ~2 kcal mol<sup>−1</sup> compared to MRCI. The AQZ-DK-MRCI and AQZ-DK-MRCI+Q *D*<sub>e</sub>s are only ~1 kcal mol<sup>−1</sup> lower compared to the AQZ-MRCI and AQZ-MRCI+Q for FeH<sup>+</sup>(X<sup>5</sup>Δ). Under all utilized CCSD(T) levels, the *D*<sub>e</sub>s of FeH<sup>+</sup> are ~54 kcal mol<sup>−1</sup>. The zero-point energy corrected binding energy of FeH<sup>+</sup> under our largest non-relativistic level of theory c-A5Z-CCSD(T) is 51.79 kcal mol<sup>−1</sup>. This value is ~1.5 kcal mol<sup>−1</sup> greater than the upper bound of the *D*<sub>0</sub> value of the experimental study by Elkind and Armentrout (*i.e.*, 48.9 ± 1.4 kcal mol<sup>−1</sup>).<sup>5</sup> The AQZ-DK-MRCI+Q *D*<sub>0</sub> is closer to the c-A5Z-CCSD(T) *D*<sub>0</sub> (*i.e.*, 51.57 versus 51.79 kcal mol<sup>−1</sup>). The AQZ-DK-MRCI *D*<sub>0</sub> is 1.95 kcal mol<sup>−1</sup> lower compared to the AQZ-DK-MRCI+Q *D*<sub>0</sub> of FeH<sup>+</sup>(X<sup>5</sup>Δ). Similar to the ground state, all *D*<sub>e</sub>s predicted by the 3 CCSD(T) approaches are in between their AQZ-MRCI and AQZ-MRCI+Q values for both A<sup>5</sup>Π and B<sup>5</sup>Σ<sup>+</sup>. Overall, 10 electronic states of FeH<sup>+</sup> bear positive *D*<sub>e</sub>s compared to the ground state fragments [*i.e.*, Fe<sup>+</sup>(<sup>6</sup>D) + H(<sup>2</sup>S) fragments].

The c-A5Z-CCSD(T) predicted *r*<sub>e</sub> of FeH<sup>+</sup> (X<sup>5</sup>Δ) is 1.578 Å which is slightly shorter compared to the *r*<sub>e</sub>s of core electron correlation disregarded approaches (~1.59 Å). The same pattern was observed for the A<sup>5</sup>Π and B<sup>5</sup>Σ<sup>+</sup> states as well. The observation of the tendency of core electron correlation to shorten the *r*<sub>e</sub>s is in agreement with our past experiences of transition metal-based diatomic species.<sup>57–61</sup> This is due to the electron excitation from core-to-virtual orbitals which further exposes the nuclear charge of Fe<sup>+</sup> to a favorable attraction with the valence electron of H. The implementation of relativistic effects decreased the *r*<sub>e</sub>s of FeH<sup>+</sup> slightly. Specifically, the discrepancies between the AQZ-MRCI/AQZ-MRCI+Q versus AQZ-DK-MRCI/AQZ-DK-MRCI+Q are less than 0.03 Å. Among the chemically bound states, the longest *r*<sub>e</sub> was observed for the B<sup>5</sup>Σ<sup>+</sup> state, which is the only state to host 2 electrons in the 7σ orbital (note: the states with shallow minima are disregarded). The discrepancy between AQZ-MRCI and AQZ-MRCI+Q *T*<sub>e</sub>s is less than 570 cm<sup>−1</sup> (Table 2). For all states, the AQZ-MRCI+Q predicted *T*<sub>e</sub>s are higher than the AQZ-MRCI

(by 230–570 cm<sup>−1</sup>) except for the first 2 excited state of FeH<sup>+</sup> in which the AQZ-MRCI+Q predicted 45 and 162 cm<sup>−1</sup> lower *T*<sub>e</sub>s respectively compared to the AQZ-MRCI. Importantly, both AQZ-MRCI and AQZ-MRCI+Q provided the same ordering for all the electronic states reported in the present work. Among the available relativistic data, the discrepancy between AQZ-DK-MRCI and AQZ-DK-MRCI+Q *T*<sub>e</sub>s is less than 400 cm<sup>−1</sup>.

Overall, our results are in good agreement with the findings reported for the first few states of FeH<sup>+</sup> by Cheng and DeYonker (Table 2 and ref. 10). The IE of FeH reported by Cheng and DeYonker under a focal point analysis (*i.e.*, 7.4851 eV) is also in good agreement with our adiabatic IEs [*i.e.*, 7.244, 7.263, and 7.425 eV at AQZ-CCSD(T), A5Z-CCSD(T), and c-A5Z-CCSD(T) levels, respectively].<sup>10</sup>

The spin-orbit coupling effects of FeH<sup>+</sup> were evaluated by including the X<sup>5</sup>Δ, A<sup>5</sup>Π, B<sup>5</sup>Σ<sup>+</sup>, a<sup>3</sup>Σ<sup>−</sup>, b<sup>3</sup>Φ, c<sup>3</sup>Π, and d<sup>3</sup>Δ electronic states of FeH<sup>+</sup> in the spin-orbit matrix. These electronic states produce Ω = 4, 3, 2, 1, 0<sup>+</sup>, and 0<sup>−</sup> (X<sup>5</sup>Δ), Ω = 3, 2, 1, 1, 0<sup>+</sup>, and 0<sup>−</sup> (A<sup>5</sup>Π), Ω = 2, 1, and 0<sup>+</sup> (B<sup>5</sup>Σ<sup>+</sup>), Ω = 1 and 0<sup>−</sup> (a<sup>3</sup>Σ<sup>−</sup>), Ω = 4, 3, and 2 (b<sup>3</sup>Φ), Ω = 2, 1, 0<sup>+</sup>, and 0<sup>−</sup> (c<sup>3</sup>Π), and Ω = 3, 2, and 1 (d<sup>3</sup>Δ). The spin-orbit curves of these states are depicted in the Fig. 2. Their *r*<sub>e</sub>, *T*<sub>e</sub>, ω<sub>e</sub> and ΛS compositions are given in the Table 3. The Ω products of the X<sup>5</sup>Δ span within 0–703 cm<sup>−1</sup>. The ground spin-orbit state of FeH<sup>2+</sup> is indeed the Ω = 4 component of the X<sup>5</sup>Δ. The *r*<sub>e</sub> and the ω<sub>e</sub> of the Ω = 4 ground state are slightly different from those of the parent X<sup>5</sup>Δ electronic state (Tables 2 and 3). The Ω = 4 ground spin-orbit state is 413 cm<sup>−1</sup> more stabilized compared to the X<sup>5</sup>Δ of FeH<sup>+</sup>.

Accurate μ values are vital for calculating radiative characteristics, spectra, and opacities of molecules. Aiming to aid such future studies, here we report MRCI and CCSD(T) μ values of several low-lying electronic states of FeH<sup>+</sup> (Table 2). Among all states (at equilibrium distances) the largest μ was observed for the ground state of FeH<sup>+</sup> [~2.3 D at AQZ-MRCI, AQZ-DK-MRCI, and c-A5Z-CCSD(T)] (Table 2). This value is ~0.1 D smaller than the MCPF μ reported by Lars *et al.* in 1987 (*i.e.*, 2.41 D).<sup>7</sup> The relativistic effects caused a minor change in μ (Table 2). Specifically, the largest difference between AQZ-MRCI versus AQZ-DK-MRCI was observed for the d<sup>3</sup>Δ state and it is only 0.12 D. Upon comparison of non-relativistic analysis, AQZ-MRCI μ versus c-A5Z-CCSD(T) μ of each X<sup>5</sup>Δ, A<sup>5</sup>Π, and B<sup>5</sup>Σ<sup>+</sup> are in better agreement and the discrepancies are less than 0.1 D. The AQZ-CCSD(T) and A5Z-CCSD(T) are very close to each other (Table 2) but they are 0.1–0.2 D larger compared to c-A5Z-CCSD(T) μ values.

Here we further report μ of FeH<sup>+</sup> (X<sup>5</sup>Δ) under a series of exchange correlation functionals that span multiple rungs of Jacob's ladder of DFA aiming to assess its density functional theory errors. Specifically, we used GGAs (BP86,<sup>29,30</sup> BLYP,<sup>31,32</sup> PBE<sup>33</sup>), MGGAs (TPSS,<sup>34</sup> MN15-L<sup>35</sup>), global GGA hybrids (B3LYP,<sup>36–38</sup> B3P86,<sup>29,36</sup> B3PW91,<sup>36,39</sup> PBE0<sup>40</sup>), MGGAs hybrids (TPSSH,<sup>34</sup> M06-2X,<sup>41</sup> MN15<sup>42</sup>), RSHs (LRC-ωPBE,<sup>43</sup> CAM-B3LYP,<sup>44</sup> ωB97X<sup>45</sup>), and DHs (PBE0-DH,<sup>46</sup> DSDPBEP86<sup>47,48</sup>). We utilized the AQZ-CCSD(T) total μ (2.50 D) of FeH<sup>+</sup> (X<sup>5</sup>Δ) to assess DFT errors since DFT calculations were also performed under the AQZ basis set. We see a general trend of improvement of μ, when moving



**Table 2** Adiabatic dissociation energy with respect to the  $\text{Fe}^+(\text{}^6\text{D}) + \text{H}(\text{}^2\text{S})$  fragments  $D_e$  (kcal mol $^{-1}$ ), bond length  $r_e$  (Å), excitation energy  $T_e$  (cm $^{-1}$ ), harmonic vibrational frequency  $\omega_e$  (cm $^{-1}$ ), anharmonicity  $\omega_e x_e$  (cm $^{-1}$ ), equilibrium rotational constant  $B_e$  (cm $^{-1}$ ), anharmonic correction to the rotational constant  $\alpha_e$  (cm $^{-1}$ ), centrifugal distortion constant  $\bar{D}_e$  (cm $^{-1}$ ), and dipole moment ( $\mu$ ) at the equilibrium distance of the 27 low-lying electronic states of  $\text{FeH}^+$

State	Level of theory	$D_e$	$r_e$	$T_e$	$\omega_e$	$\omega_e x_e$	$B_e$	$\alpha_e$	$\bar{D}_e$	$\mu$
$\text{X}^5\Delta$	AQZ-MRCI	53.27	1.586	—	1844	34.1	6.765	0.1794	0.000385	−2.31
	AQZ-MRCI+Q	55.24	1.587	—	1862	30.6	6.758	0.1736	0.000357	—
	AQZ-DK-MRCI	52.23	1.581	—	1849	34.9	6.818	0.1878	0.000370	−2.26
	AQZ-DK-MRCI+Q	54.22	1.582	—	1870	32.6	6.802	0.1864	0.000359	—
	AQZ-CCSD(T)	53.90	1.590	—	1852	30.5	6.752	0.1884	0.000352	−2.50
	A5Z-CCSD(T)	54.18	1.589	—	1852	30.5	6.743	0.1889	0.000356	−2.50
	c-A5Z-CCSD(T)	54.44	1.578	—	1865	30.5	6.834	0.1703	0.000365	−2.34
	MRCI $^{10}$		1.5944		1836					
	MRCI+Q $^{10}$		1.5891		1848					
	CCSDT $^{10}$		1.5882		1850.4	32.2	6.7508	0.1761	0.000359	
	CCSDTQ $^{10}$		1.5882		1849.8	32.3	6.7524	0.1765	0.000360	
	FPA $^{10}$		1.5736	—	1874.2	31.9	6.8766	0.1798	0.000370	
	AQZ-MRCI	51.07	1.569	768	1820	34.7	6.906	0.1888	0.000401	−2.14
	AQZ-MRCI+Q	53.18	1.570	723	1843	30.9	6.911	0.1852	0.000386	—
$\text{A}^5\Pi$	AQZ-DK-MRCI	50.66	1.563	550	1829	33.7	6.974	0.1984	0.000404	−2.08
	AQZ-DK-MRCI+Q	52.77	1.563	507	1857	33.5	6.975	0.1972	0.000396	—
	AQZ-CCSD(T)	51.87	1.575	710	1826	31.1	6.895	0.1755	0.000386	−2.34
	A5Z-CCSD(T)	52.12	1.574	718	1827	31.4	6.878	0.1744	0.000387	−2.34
	c-A5Z-CCSD(T)	52.10	1.564	819	1845	30.8	6.857	0.1784	0.000396	−2.19
	MRCI $^{10}$		1.5780		1821					
	MRCI+Q $^{10}$		1.5711		1837					
	CCSDT $^{10}$		1.5699		1835.9	32.7	6.9088	0.1861	0.000391	
	CCSDTQ $^{10}$		1.5697		1835.0	32.8	6.9105	0.1866	0.000392	
	FPA $^{10}$		1.5558	601	1859.4	31.7	7.0351	0.1898	0.000402	
	AQZ-MRCI	40.69	1.637	4401	1709	37.3	6.347	0.1879	0.000352	−2.23
	AQZ-MRCI+Q	43.12	1.633	4239	1722	32.4	6.389	0.1807	0.000358	—
	AQZ-DK-MRCI	41.64	1.620	3703	1712	37.7	6.491	0.2052	0.000372	−2.10
	AQZ-DK-MRCI+Q	44.09	1.615	3540	1750	33.4	6.527	0.2057	0.000363	—
$\text{B}^5\Sigma^+$	AQZ-CCSD(T)	42.75	1.635	3902	1727	33.3	6.368	0.1797	0.000346	−2.48
	A5Z-CCSD(T)	42.84	1.635	3965	1727	33.4	6.370	0.1820	0.000347	−2.45
	c-A5Z-CCSD(T)	42.28	1.630	4253	1730	32.7	6.411	0.1838	0.000352	−2.31
	AQZ-MRCI	25.19	1.497	9821	1938	71.1	7.703	0.4284	0.000624	−1.40
	AQZ-MRCI+Q	26.34	1.497	10 109	1897	69.7	7.603	0.3068	0.000488	—
	AQZ-DK-MRCI	20.92	1.489	10 949	1959	61.8	7.680	0.3714	0.000561	−1.49
	AQZ-DK-MRCI+Q	22.13	1.489	11 223	1974	58.7	7.679	0.3622	0.000547	—
	MRCI $^{10}$		1.4907		1922					
	MRCI+Q $^{10}$		1.4944		1901					
	CCSDT $^{10}$		1.4831		2000.3	47.6	7.7419	0.2522	0.000464	
	CCSDTQ $^{10}$		1.4862		1977.1	49.6	7.7093	0.2598	0.000469	
	FPA $^{10}$		1.4821	10 081	1965.0	51.0	7.7530	0.2745	0.000481	
	AQZ-MRCI	22.29	1.517	10 835	1886	92.0	7.515	0.4764	0.000653	−1.34
	AQZ-MRCI+Q	23.29	1.517	11 175	1844	81.9	7.395	0.4341	0.000475	—
	AQZ-DK-MRCI	18.22	1.509	11 896	1906	87.4	7.574	0.4006	0.000578	−1.45
$\text{a}^3\Sigma^-$	AQZ-DK-MRCI+Q	19.27	1.509	12 222	1922	84.6	7.566	0.3915	0.000569	—
	AQZ-MRCI	19.26	1.533	11 896	1824	99.1	7.399	0.5214	0.000635	−1.37
	AQZ-MRCI+Q	20.30	1.532	12 222	1769	83.4	7.253	0.3544	0.000488	—
	AQZ-DK-MRCI	15.48	1.520	12 853	1839	92.5	7.473	0.4255	0.000600	−1.46
$\text{c}^3\Pi$	AQZ-DK-MRCI+Q	16.58	1.520	13 162	1866	89.1	7.469	0.4139	0.000599	—
	AQZ-MRCI	10.21	1.599	15 063	1581	108.0	6.637	0.4950	0.000694	−1.16
	AQZ-MRCI+Q	11.10	1.598	15 438	1513	97.7	6.670	0.3950	0.000518	—
	AQZ-DK-MRCI	7.15	1.574	15 765	1617	111.5	6.876	0.5075	0.000712	−1.28
$\text{d}^3\Delta$	AQZ-DK-MRCI+Q	8.13	1.573	16 120	1658	96.3	6.883	0.4891	0.000723	—
	AQZ-MRCI	2.05	2.079	17 915	—	—	—	—	—	—
	AQZ-MRCI+Q	2.52	2.061	18 442	—	—	—	—	—	—
	AQZ-DK-MRCI	1.47	2.149	18 118	—	—	—	—	—	—
$1^5\Sigma^-$	AQZ-MRCI+Q	1.86	2.133	18 671	—	—	—	—	—	—
	AQZ-MRCI	0.71	2.171	18 384	—	—	—	—	—	—
$1^5\Phi$	AQZ-MRCI+Q	1.13	2.149	18 926	—	—	—	—	—	—
	AQZ-MRCI	—	2.297	18 862	—	—	—	—	—	—
$2^5\Pi$	AQZ-MRCI+Q	—	2.267	19 424	—	—	—	—	—	—
	AQZ-MRCI	—	1.534	20 288	1824	66.9	7.399	0.5214	0.000735	—
$2^5\Delta$	AQZ-MRCI+Q	—	1.532	20 527	1811	71.5	7.259	0.5462	0.000813	—
	AQZ-MRCI	—	1.546	20 591	1959	22.4	7.121	0.4947	0.000376	—
$1^3\text{H}$	AQZ-MRCI+Q	—	1.545	21 002	1898	31.4	7.132	0.4183	0.000413	—
	AQZ-MRCI	—	1.473	21 215	1928	28.0	7.803	0.2190	0.000482	—
$2^3\Pi$	AQZ-MRCI+Q	—	1.472	21 600	2016	29.7	7.855	0.2223	0.000477	—
	AQZ-MRCI	—	1.485	21 330	2085	62.2	7.735	0.2492	0.000457	—



Table 2 (continued)

State	Level of theory	$D_e$	$r_e$	$T_e$	$\omega_e$	$\omega_e x_e$	$B_e$	$\alpha_e$	$\bar{D}_e$	$\mu$
$1^3\Gamma$	AQZ-MRCI+Q	—	1.485	21 722	2014	54.7	7.768	0.2580	0.000463	—
	AQZ-MRCI	—	1.581	21 526	1793	28.9	6.866	0.1694	0.000415	—
	AQZ-MRCI+Q	—	1.580	21 939	1755	30.1	6.825	0.1607	0.000413	—
$2^3\Delta$	AQZ-MRCI	—	1.580	21 540	1746	38.9	6.821	0.2613	0.000406	—
	AQZ-MRCI+Q	—	1.581	21 954	1795	41.9	6.813	0.2814	0.000393	—
	AQZ-MRCI	—	1.562	21 733	1807	31.5	6.892	0.2360	0.000512	—
$2^3\Sigma^-$	AQZ-MRCI+Q	—	1.561	22 114	1801	29.7	6.884	0.1976	0.000489	—
	AQZ-MRCI	—	1.581	22 430	1823	36.0	6.826	0.1877	0.000411	—
	AQZ-MRCI+Q	—	1.580	22 809	1831	36.1	6.839	0.1862	0.000404	—
$3^3\Sigma^-$	AQZ-MRCI	—	1.598	22 629	1769	55.9	6.684	0.2353	0.000326	—
	AQZ-MRCI+Q	—	1.597	22 919	1780	52.5	6.680	0.2188	0.000376	—
$1^1\Pi$	AQZ-MRCI	—	1.508	22 978	1918	46.4	7.482	0.2334	0.000457	—
	AQZ-MRCI+Q	—	1.507	23 379	1924	46.6	7.501	0.2448	0.000456	—
$2^3\Phi$	AQZ-MRCI	—	1.570	23 521	1686	38.6	6.867	0.2403	0.000433	—
	AQZ-MRCI+Q	—	1.568	23 885	1744	36.2	6.839	0.2161	0.000404	—
$3^3\Delta$	AQZ-MRCI	—	1.591	24 552	1761	35.6	6.725	0.1956	0.000392	—
	AQZ-MRCI+Q	—	1.589	24 897	1771	36.5	6.745	0.1960	0.000391	—
$3^5\Delta$	AQZ-MRCI	—	2.649	24 745	—	—	—	—	—	—
	AQZ-MRCI+Q	—	2.603	25 168	—	—	—	—	—	—
$3^5\Pi$	AQZ-MRCI	—	2.613	24 794	—	—	—	—	—	—
	AQZ-MRCI+Q	—	2.569	25 232	—	—	—	—	—	—
$2^5\Sigma^+$	AQZ-MRCI	—	2.707	24 938	—	—	—	—	—	—
	AQZ-MRCI+Q	—	2.678	25 404	—	—	—	—	—	—
$1^1\Phi$	AQZ-MRCI	—	1.522	25 851	1884	28.9	7.311	0.2061	0.000440	—
	AQZ-MRCI+Q	—	1.520	26 242	1831	28.6	7.366	0.2087	0.000440	—

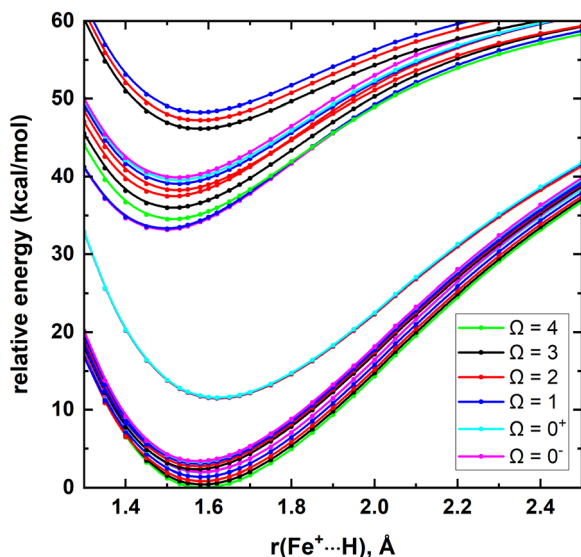


Fig. 2 AQZ-DK-MRCI spin-orbit coupling curves resulting from  $X^5\Delta$ ,  $A^5\Pi$ ,  $B^5\Sigma^+$ ,  $a^3\Sigma^-$ ,  $b^3\Phi$ ,  $c^3\Pi$ , and  $d^3\Delta$  electronic states of  $FeH^+$  as a function of  $Fe^+\cdots H$  distance [ $r(Fe^+\cdots H)$ , Å]. The relative energies are referenced with respect to the  $\Omega = 4$  ground state minimum of  $FeH^+$ . The  $\Omega = 4$ ,  $\Omega = 3$ ,  $\Omega = 2$ ,  $\Omega = 1$ ,  $\Omega = 0^+$ , and  $\Omega = 0^-$  curves are shown in green, black, red, blue, cyan, and pink, respectively. See Fig. 1 for the PEC of their parent electronic states.

from lower to higher rungs of DFA (ESI,† Fig. S2 and Table S1). Compared to CCSD(T), the more expensive DHs (PBE0-DH and DSDPBEP86) overestimated  $\mu$  by  $\sim 5$  and 13% (ESI,† Table S1). All 3 functionals of RSH predicted  $\mu$  values with less than 9% of errors. The MGGA hybrid M06-2X  $\mu$  is almost identical to the AQZ-CCSD(T)  $\mu$  value (2.53 versus 2.50 D) and this is the best

Table 3 Bond length  $r_e$  (Å), excitation energy  $T_e$  ( $cm^{-1}$ ), harmonic vibrational frequency  $\omega_e$  ( $cm^{-1}$ ), and %  $\Lambda S$  composition of several low-lying spin-orbit states of  $FeH^+$  at AQZ-DK-MRCI level

$\Omega$	$r_e$	$T_e$	$\omega_e$	$\Lambda S$ composition <sup>a</sup>
4	1.586	0	1859	100% $X^5\Delta$
3	1.584	139	1868	89% $X^5\Delta$ + 11% $A^5\Pi$
2	1.583	288	1800	82% $X^5\Delta$ + 18% $A^5\Pi$
1	1.582	479	1797	75% $X^5\Delta$ + 25% $A^5\Pi$
$0^+$	1.581	688	1792	68% $X^5\Delta$ + 31% $A^5\Pi$
$0^-$	1.581	703	1794	73% $X^5\Delta$ + 27% $A^5\Pi$
3	1.570	812	1844	89% $A^5\Pi$ + 11% $X^5\Delta$
2	1.572	949	1851	81% $A^5\Pi$ + 18% $X^5\Delta$
1	1.573	1063	1861	76% $A^5\Pi$ + 23% $X^5\Delta$
1	1.568	1130	1784	98% $A^5\Pi$ + 2% $X^5\Delta$
$0^+$	1.573	1134	1884	67% $A^5\Pi$ + 32% $X^5\Delta$ + 1% $B^5\Sigma^+$
$0^-$	1.573	1174	1872	73% $A^5\Pi$ + 27% $X^5\Delta$
2	1.623	4005	1725	100% $B^5\Sigma^+$
1	1.622	4033	1724	99% $B^5\Sigma^+$ + 1% $A^5\Pi$
$0^+$	1.622	4042	1728	98% $B^5\Sigma^+$ + 2% $A^5\Pi$
$0^-$	1.492	11 577	1930	95% $a^3\Sigma^-$ + 5% $c^3\Pi$
1	1.492	11 628	1938	97% $a^3\Sigma^-$ + 3% $c^3\Pi$
4	1.511	12 060	1893	100% $b^3\Phi$
3	1.511	12 574	1894	100% $b^3\Phi$
2	1.511	13 093	1890	100% $b^3\Phi$
2	1.522	13 366	1828	100% $c^3\Pi$
1	1.522	13 654	1842	96% $c^3\Pi$ + 3% $a^3\Sigma^-$
$0^-$	1.523	13 818	1834	100% $c^3\Pi$
$0^+$	1.521	13 941	1847	95% $c^3\Pi$ + 5% $a^3\Sigma^-$
3	1.577	16 136	1627	100% $d^3\Delta$
2	1.577	16 514	1624	99% $d^3\Delta$
1	1.577	16 877	1619	100% $d^3\Delta$

<sup>a</sup> Only components that are equal or larger than 1% are listed.

performing functional for  $\mu$  of  $FeH^+(X^5\Delta)$  among all 17 DFAs. The errors of global GGA hybrids span in between 9–17%. The MGGA MN15-L is a clear outlier of the linear-like  $\mu$  improving trend going from GGA to DHs. However, the MN15-L  $\mu$  is closer to



the AQZ-CCSD(T)  $\mu$  than for any functional of GGA. The largest deviation of DFT  $\mu$  compared to the AQZ-CCSD(T) was observed for the least expensive GGAs with approximate errors of 30% (ESI,† Table S1). Overall, our general expectation that the more expensive functionals from the higher rungs of the Jacob's ladder of DFA would perform better compared to the ones at the lower rungs holds true for the  $\mu$  of  $\text{FeH}^+(\text{X}^5\Delta)$ .<sup>18</sup>

The DMC of the first 7 electronic states of  $\text{FeH}^+$  obtained at the MRCI level are illustrated in the Fig. 3a. Among the focused range, the largest total  $\mu$  was observed for the  $\text{B}^5\Sigma^+$  (2.5 D) around 1.3 Å. The DMC minima of  $\text{X}^5\Delta$  and  $\text{A}^5\Pi$  were observed at  $\sim 1.5$  Å with  $-2.4$  and  $-2.2$  D, respectively. The DMC of all 4 triplet-spin

states (*i.e.*,  $\text{b}^3\Phi$ ,  $\text{c}^3\Pi$ ,  $\text{d}^3\Delta$ , and  $\text{a}^3\Sigma^-$ ) are qualitatively and quantitatively similar throughout the scale and they reach the minimization around the 1.3–1.4 Å. Note that for all states, the DMC minima were observed at slightly shorter  $\text{Fe}^+\cdots\text{H}$  distances compared to their equilibrium distances (Fig. 1 and 3). The TDMC arising from the lowest 7 states of  $\text{FeH}^+$  are given in Fig. 3b. Among the studied quintet-spin states (*i.e.*,  $\text{X}^5\Delta$ ,  $\text{A}^5\Pi$ , and  $\text{B}^5\Sigma^+$ ) the  $\text{X}^5\Delta \leftrightarrow \text{A}^5\Pi$  and  $\text{B}^5\Sigma^+ \leftrightarrow \text{A}^5\Pi$  transitions are permitted, whereas the transition between  $\text{X}^5\Delta \leftrightarrow \text{B}^5\Sigma^+$  is forbidden. The largest transition  $\mu$  values of  $\text{X}^5\Delta \leftrightarrow \text{A}^5\Pi$  and  $\text{B}^5\Sigma^+ \leftrightarrow \text{A}^5\Pi$  were observed at approximately 1.6 and 1.3 Å and they are only 0.08 and 0.11 D, respectively. The  $\text{d}^3\Delta \leftrightarrow \text{c}^3\Pi$ ,  $\text{a}^3\Sigma^- \leftrightarrow \text{c}^3\Pi$ , and  $\text{d}^3\Delta \leftrightarrow \text{b}^3\Phi$  transitions are allowed for the studied triplet-spin states of  $\text{FeH}^+$  and the corresponding transition  $\mu$  values are increasing with the compression of the  $\text{Fe}^+\cdots\text{H}$  distance.

### III.B. $\text{FeH}^{2+}$

The removal of the  $4s^1$  valence electron from the  $\text{Fe}^+$  ( $^6\text{D}$ ;  $[\text{Ar}]3\text{d}^64s^1$ ) produces the ground electronic state of  $\text{Fe}^{2+}$  ( $^5\text{D}$ ;  $[\text{Ar}]3\text{d}^6$ ).<sup>53</sup> The low energy electronic spectrum of  $\text{Fe}^{2+}$  is much less dense compared to the spectrum of  $\text{Fe}^+$ . For example, the first excited state of  $\text{Fe}^{2+}$  ( $^3\text{P}$ ;  $[\text{Ar}]3\text{d}^6$ ) lies 55.48–60.64 kcal mol<sup>−1</sup> above, whereas  $\text{Fe}^+$  populates 5 excited states within 0–55 kcal mol<sup>−1</sup> range.<sup>53</sup> Since the excitation energies of  $\text{Fe}^{2+}$  are relatively high in energy, in the present work we have only considered the reaction between the ground state of  $\text{Fe}^{2+}$  ( $^5\text{D}$ ) and  $\text{H}(^2\text{S})$ . According to the Wigner–Witmer rules, this combination produces  $^6, ^4[\Sigma^+, \Pi, \Delta]$  electronic states. Here all of these states were analyzed under the MRCI level of theory.<sup>54,55</sup> Similar to  $\text{FeH}^+$ , the CASSCF active space used for MRCI calculations of  $\text{FeH}^{2+}$  was constructed from the

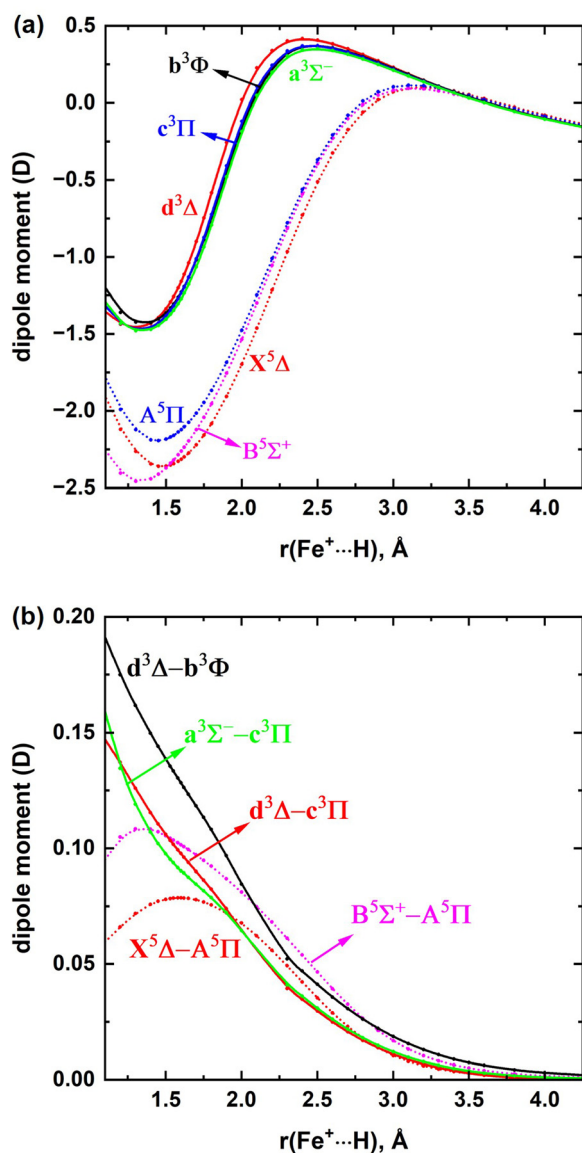


Fig. 3 (a) MRCI/aug-cc-pVQZ DMC of  $\text{FeH}^+$  as a function of  $\text{Fe}^+\cdots\text{H}$  distance [ $r(\text{Fe}^+\cdots\text{H})$ , Å]. The solid and dotted DMC correspond to the triplet and quintet spins, respectively. The  $\Delta$ ,  $\Pi$ ,  $\Sigma^+$ ,  $\Sigma^-$ , and  $\Phi$  states are shown in red, blue, pink, green, and black, respectively. (b) MRCI/aug-cc-pVQZ TDMC resulting from  $\text{X}^5\Delta \leftrightarrow \text{A}^5\Pi$ ,  $\text{B}^5\Sigma^+ \leftrightarrow \text{A}^5\Pi$ ,  $\text{d}^3\Delta \leftrightarrow \text{c}^3\Pi$ ,  $\text{a}^3\Sigma^- \leftrightarrow \text{c}^3\Pi$ , and  $\text{d}^3\Delta \leftrightarrow \text{b}^3\Phi$  of  $\text{FeH}^+$  as a function of  $\text{Fe}^+\cdots\text{H}$  distance [ $r(\text{Fe}^+\cdots\text{H})$ , Å].

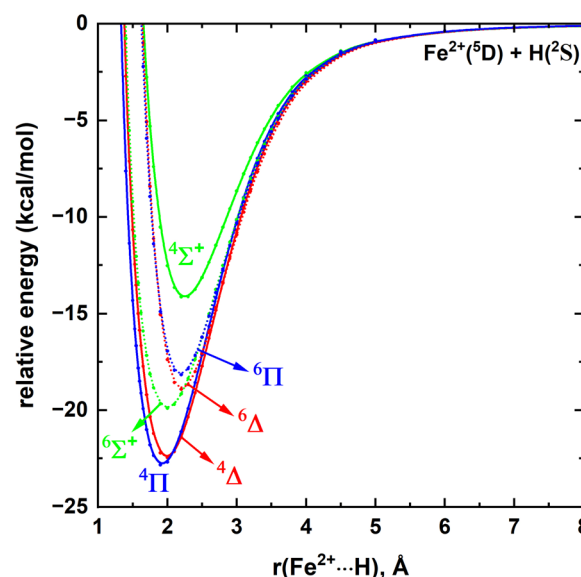


Fig. 4 MRCI/aug-cc-pVQZ PEC of  $\text{FeH}^{2+}$  as a function of  $\text{Fe}^{2+}\cdots\text{H}$  distance [ $r(\text{Fe}^{2+}\cdots\text{H})$ , Å]. The relative energies are with respect to the total energy of  $\text{Fe}^{2+}(^5\text{D}) + \text{H}(^2\text{S})$  when they are at 200 Å separation, which is set to 0 kcal mol<sup>−1</sup>. The solid and dotted PEC correspond to the quartet and sextet spins, respectively. The  $\Delta$ ,  $\Pi$ , and  $\Sigma^+$  states are shown in red, blue, and green, respectively.





five 3d, five 4d, and the 4s orbitals of Fe and the 1s orbital of H [CAS(7,12)]. The full PEC of the 6 electronic states of  $\text{FeH}^{2+}$  studied are given in the Fig. 4.

All PEC are attractive in nature with  $\sim 14\text{--}23\text{ kcal mol}^{-1} D_e$ . According to the MRCI potential energy profile, the ground state of  $\text{FeH}^{2+}$  is a  $^4\Pi$  state, followed very closely by a  $^4\Delta$  state (Fig. 4). The two most stable states of  $\text{FeH}^{2+}$  ( $^4\Pi$  and  $^4\Delta$ ) are

**Table 4** Dominant electronic configurations at the equilibrium distances of the 6 low-lying electronic states of  $\text{FeH}^{2+}$

State <sup>a</sup>	Coefficient <sup>b</sup>	Configuration <sup>c</sup>
$^4\Pi$	0.74	$6\sigma^2 3\pi_x^2 3\pi_y(1\delta_{x^2-y^2})1\delta_{xy}$
	−0.43	$7\sigma^2 3\pi_x^2 3\pi_y(1\delta_{x^2-y^2})1\delta_{xy}$
$^4\Delta$	0.73	$6\sigma^2 3\pi_x 3\pi_y(1\delta_{x^2-y^2})^2 1\delta_{xy}$
	−0.44	$7\sigma^2 3\pi_x 3\pi_y(1\delta_{x^2-y^2})^2 1\delta_{xy}$
$^6\Sigma^+$	0.99	$6\sigma^2 7\sigma 3\pi_x 3\pi_y(1\delta_{x^2-y^2})1\delta_{xy}$
$^6\Delta$	0.99	$6\sigma 7\sigma 3\pi_x 3\pi_y(1\delta_{x^2-y^2})^2 1\delta_{xy}$
$^6\Pi$	0.99	$6\sigma 7\sigma 3\pi_x^2 3\pi_y(1\delta_{x^2-y^2})1\delta_{xy}$
$^4\Sigma^+$	0.83	$6\sigma^2 7\sigma 3\pi_x 3\pi_y(1\delta_{x^2-y^2})1\delta_{xy}$
	−0.32	$6\sigma 7\sigma^2 3\pi_x 3\pi_y(1\delta_{x^2-y^2})1\delta_{xy}$

<sup>a</sup> The corresponding  $A_1$  (of  $\Delta$ ) and  $B_1$  (of  $\Pi$ ) components under  $C_{2v}$  symmetry are listed. <sup>b</sup> All the CI coefficients that are larger than 0.3 of corresponding natural orbital representations are given. <sup>c</sup>  $\beta$  and  $\alpha$ -spin electrons are specified with and without bars over the spatial orbital, respectively.

multireference in nature (Table 4). The electronic configurations of the two main components of the  $^4\Pi$  state are  $6\sigma^2 3\pi^3 1\delta^2$  (55%) and  $7\sigma^2 3\pi^3 1\delta^2$  (18%). Notice that the major configuration of  $^4\Pi$  state ( $6\sigma^2 3\pi^3 1\delta^2$ ) can be produced by eliminating the  $7\sigma^1$  electron from the  $A^5\Pi$  of  $\text{FeH}^+$  ( $6\sigma^2 7\sigma^1 3\pi^3 1\delta^2$ ). The MRCI and MRCI+Q predicted IEs of this process are 17.0 and 17.2 eV, respectively. On the other hand, the dominant configuration of the  $^4\Delta$  ( $6\sigma^2 3\pi^2 1\delta^3$ ) is the  $7\sigma^1$  electron ionized product of the  $\text{FeH}^+$  ( $X^5\Delta$ ;  $6\sigma^2 7\sigma^1 3\pi^2 1\delta^3$ ). The next 3 states of  $\text{FeH}^{2+}$  carry single-reference electronic configurations and hence those were further analyzed with CCSD(T) levels of theory. All our CCSD(T) and MRCI numerical findings of  $\text{FeH}^{2+}$  are listed in Table 5.

The  $D_e$  of  $\text{FeH}^{2+}(^4\Pi)$  under AQZ-MRCI and AQZ-MRCI+Q levels are 22.85 and 23.13  $\text{kcal mol}^{-1}$ . The zero-point energy corrected AQZ-MRCI and AQZ-MRCI+Q  $D_0$ s of  $\text{FeH}(^4\Pi)$  are 21.66 and 21.94  $\text{kcal mol}^{-1}$ . Under both AQZ-MRCI and AQZ-MRCI+Q levels the  $^4\Delta$  state lies only 0.4  $\text{kcal mol}^{-1}$  above the  $^4\Pi$  (Table 5) (*i.e.*, the AQZ-MRCI and AQZ-MRCI+Q  $D_0$  of  $^4\Delta$  are 21.29 and 21.49, respectively). Our MRCI+Q is only 1  $\text{kcal mol}^{-1}$  larger than the MRCI+Q  $D_e$  of  $^4\Delta$  reported by Wilson *et al.* in 2003 (22.68 *versus* 21.68  $\text{kcal mol}^{-1}$ ).<sup>12</sup> Our AQZ-DK-MRCI and AQZ-DK-MRCI+Q  $D_0$  values of  $\text{FeH}^{2+}(^4\Pi)$  are 22.27 and 22.57  $\text{kcal mol}^{-1}$ , respectively. The introduction of the relativistic effects only increased the  $D_0$  of  $\text{FeH}^{2+}(^4\Pi)$  by  $\sim 1\text{ kcal mol}^{-1}$ .

**Table 5** Adiabatic dissociation energy with respect to the  $\text{Fe}^{2+}(^5D) + \text{H}(^2S)$  fragments  $D_e$  ( $\text{kcal mol}^{-1}$ ), bond length  $r_e$  (Å), excitation energy  $T_e$  ( $\text{cm}^{-1}$ ), harmonic vibrational frequency  $\omega_e$  ( $\text{cm}^{-1}$ ), anharmonicity  $\omega_e x_e$  ( $\text{cm}^{-1}$ ), equilibrium rotational constant  $B_e$  ( $\text{cm}^{-1}$ ), anharmonic correction to the rotational constant  $\alpha_e$  ( $\text{cm}^{-1}$ ), centrifugal distortion constant  $\bar{D}_e$  ( $\text{cm}^{-1}$ ), and dipole moment ( $\mu$ ) at equilibrium distance of the 6 low-lying electronic states of  $\text{FeH}^{2+}$

State	Level of theory	$D_e$	$r_e$	$T_e$	$\omega_e$	$\omega_e x_e$	$B_e$	$\alpha_e$	$\bar{D}_e$	$\mu$
$^4\Pi$	AQZ-MRCI	22.85	1.923	—	841	16.3	4.604	0.1566	0.000552	1.21
	AQZ-MRCI+Q	23.13	1.918	—	846	16.2	4.639	0.1574	0.000529	—
	AQZ-DK-MRCI	23.47	1.908	—	848	15.8	4.690	0.1566	0.000538	1.22
	AQZ-DK-MRCI+Q	23.76	1.902	—	852	15.7	4.711	0.1157	0.000562	—
	MRCI+Q <sup>12</sup>	21.68	1.998	—	830	—	—	—	—	—
$^4\Delta$	AQZ-MRCI	22.47	1.989	135	839	17.0	4.314	0.1369	0.000455	1.36
	AQZ-MRCI+Q	22.68	1.986	156	841	17.0	4.329	0.1367	0.000453	—
	AQZ-DK-MRCI	22.95	1.977	180	842	16.5	4.368	0.1366	0.000450	1.36
	AQZ-DK-MRCI+Q	23.18	1.973	203	845	16.5	4.384	0.1364	0.000467	—
	AQZ-MRCI	19.90	1.999	1033	719	4.9	4.263	0.1503	0.000567	1.15
	AQZ-MRCI+Q	20.15	1.994	1042	727	4.4	4.297	0.1512	0.000574	—
	AQZ-DK-MRCI	21.60	1.913	654	712	11.1	4.585	0.2079	0.000768	1.05
	AQZ-DK-MRCI+Q	21.89	1.909	653	719	14.3	4.675	0.2141	0.000781	—
	AQZ-CCSD(T)	19.95	2.016	—	728	6.1	4.195	0.1144	0.000582	1.20
	A5Z-CCSD(T)	19.95	2.018	—	734	6.2	4.186	0.1129	0.000582	1.21
$^6\Delta$	c-A5Z-CCSD(T)	20.84	2.005	—	747	5.6	4.240	0.1225	0.000539	1.25
	AQZ-MRCI	18.92	2.203	1376	836	21.3	3.514	0.1370	0.000247	1.38
	AQZ-MRCI+Q	19.04	2.202	1430	836	21.2	3.516	0.1337	0.000248	—
	AQZ-DK-MRCI	19.64	2.190	1339	891	26.3	3.551	0.1180	0.000225	1.40
	AQZ-DK-MRCI+Q	19.77	2.197	1396	887	26.3	3.630	0.1129	0.000223	—
	AQZ-CCSD(T)	19.06	2.202	—	837	22.6	3.512	0.1350	0.000287	1.42
	A5Z-CCSD(T)	19.07	2.202	—	837	22.5	3.513	0.1343	0.000262	1.42
	c-A5Z-CCSD(T)	20.01	2.188	—	850	22.2	3.556	0.1331	0.000258	1.48
	AQZ-MRCI	18.17	2.187	1638	819	21.7	3.560	0.1428	0.000246	1.34
	AQZ-MRCI+Q	18.31	2.185	1687	820	21.2	3.570	0.1405	0.000269	—
$^6\Pi$	AQZ-DK-MRCI	18.96	2.171	1575	834	21.8	3.613	0.1375	0.000270	1.38
	AQZ-DK-MRCI+Q	19.11	2.169	1624	832	21.0	3.618	0.1144	0.000275	—
	AQZ-CCSD(T)	18.33	2.186	—	821	22.7	3.562	0.1404	0.000274	1.40
	A5Z-CCSD(T)	18.35	2.186	—	821	22.6	3.563	0.1391	0.000246	1.40
	c-A5Z-CCSD(T)	19.21	2.173	—	833	22.3	3.601	0.1372	0.000247	1.37
	AQZ-MRCI	14.18	2.246	3031	712	22.4	3.388	0.1484	0.000315	1.17
	AQZ-MRCI+Q	14.34	2.242	3073	716	22.1	3.389	0.1460	0.000309	—
	AQZ-DK-MRCI	14.72	2.225	3060	719	21.2	3.450	0.1450	0.000324	1.22
	AQZ-DK-MRCI+Q	14.89	2.220	3101	724	21.4	3.465	0.1448	0.000325	—



Importantly, since the energy difference between the  $^4\Pi$  and  $^4\Delta$  states is within the margin of error of the basis set and the method, it is difficult to assign a true ground state for  $\text{FeH}^{2+}$ . We performed AQZ-CCSD(T), A5Z-CCSD(T), and c-A5Z-CCSD(T) calculations for the single-reference  $^6\Sigma^+$ ,  $^6\Delta$ , and  $^6\Pi$  states of  $\text{FeH}^{2+}$ . For all these 3 states, the AQZ-CCSD(T)  $D_e$ s and A5Z-CCSD(T)  $D_e$ s are almost identical to each other (Table 5). As expected, the electron excitation from core-to-virtual orbitals [*i.e.*, c-A5Z-CCSD(T)] relaxes (or stabilizes) the electronic states increasing the  $D_e$  values approximately by 0.9 kcal mol $^{-1}$ . The bond lengths of the electronic states of  $\text{FeH}^{2+}$  are significantly longer compared to the  $r_e$ s of the states of  $\text{FeH}^+$  which translate to the lower  $D_e$ s of  $\text{FeH}^{2+}$  compared to  $\text{FeH}^+$  (compare  $r_e$ s and  $D_e$ s given in Tables 2 and 5). This also means that an apparent measured IE of  $\text{FeH}^+$  will likely be at higher energies (due to the Franck–Condon overlap). The MRCI+Q  $r_e$  of the  $^4\Delta$  state reported by Wilson *et al.*, is 0.01 Å longer compared to our MRCI+Q value.<sup>12</sup> For all states, MRCI+Q predicted slightly shorter  $r_e$ s compared to MRCI (by  $\sim 0.001$ – $0.005$  Å). Similar to the  $\text{FeH}^+$  case, the relativistic effects on the  $r_e$ s of the states of the  $\text{FeH}^{2+}$  are minor (Table 5). The c-A5Z-CCSD(T)  $r_e$ s of  $\text{FeH}^{2+}$  are shorter compared to the A5Z-CCSD(T)  $r_e$ s similar to the  $\text{FeH}^+$  case. The AQZ-MRCI+Q predicted slightly higher  $T_e$ s compared to the AQZ-MRCI  $T_e$ s (0–60 cm $^{-1}$ ). The largest discrepancy between the AQZ-DK-MRCI/AQZ-DK-MRCI+Q *versus* AQZ-MRCI/AQZ-MRCI+Q was observed for the  $^6\Sigma^+$  state which is  $\sim 400$  cm $^{-1}$ , whereas in all other cases it is less than 65 cm $^{-1}$ . Finally, we observed that all AQZ-MRCI+Q, AQZ-MRCI, AQZ-DK-MRCI, and AQZ-DK-MRCI+Q levels' predictions on spectroscopic constants agree well with each other (*i.e.*,  $\omega_e$ ,  $\omega_e x_e$ ,  $B_e$ ,  $\alpha_e$ , and  $\bar{D}_e$ ).

To investigate the spin-orbit effects of  $\text{FeH}^{2+}$ , we have included  $^4\Pi$ ,  $^4\Delta$ ,  $^6\Sigma^+$ ,  $^6\Delta$ ,  $^6\Pi$ , and  $^4\Sigma^+$  electronic states in the spin-orbit matrix. The spin-orbit coupling produces the  $\Omega = 1/2$ ,  $1/2$ ,  $3/2$ , and  $5/2$  (from  $^4\Pi$ ),  $\Omega = 1/2$ ,  $3/2$ ,  $5/2$ , and  $7/2$  (from  $^4\Delta$ ),  $\Omega = 1/2$ ,  $3/2$ , and  $5/2$  (from  $^6\Sigma^+$ ),  $\Omega = 1/2$ ,  $1/2$ ,  $3/2$ ,  $5/2$ ,  $7/2$ , and  $9/2$  (from  $^6\Delta$ ),  $\Omega = 1/2$ ,  $1/2$ ,  $3/2$ ,  $5/2$ , and  $7/2$  (from  $^6\Pi$ ), and  $\Omega = 1/2$  and  $3/2$  (from  $^4\Sigma^+$ ). The spin-orbit curves of the  $\Omega$  states are given in the Fig. 5 and the corresponding  $r_e$ ,  $T_e$ ,  $\omega_e$ , and  $\Lambda S$  compositions are listed in the Table 6. The  $\Omega$  states of the ground  $^4\Pi$  electronic states span within 0–525 cm $^{-1}$  whereas those of the first excited  $^4\Delta$  extend from 150 to 1021 cm $^{-1}$ . The ground spin-orbit state of the  $\text{FeH}^{2+}$  is an  $\Omega = 5/2$  which is stabilized over its parent  $^4\Pi$  state by 353 cm $^{-1}$ . As expected, the  $\Omega = 5/2$  ground spin-orbit state bears substantial composition of  $^4\Delta$  (20%) due to the proximity of the  $^4\Pi$  and  $^4\Delta$  states. Similarly, notable mixings were observed for many  $\Omega$  states which clearly highlights the importance of the spin-orbit coupling effects of the  $\text{FeH}^{2+}$  system (Table 6).

The AQZ-MRCI and AQZ-DK-MRCI  $\mu$  values of the  $^4\Pi$  and  $^4\Delta$  states at their  $r_e$ s are 1.2 and 1.4 D, respectively. Among all states, the largest and smallest  $\mu$  values were observed for the  $^6\Delta$  and  $^6\Sigma^+$  states, respectively (Table 5). The relativistic effects on the  $\mu$  values of  $\text{FeH}^{2+}$  are minor, where the largest difference was observed for the  $^6\Sigma^+$  state which is only 0.1 D. Similar to the  $\text{FeH}^+$  case, the  $\mu$  values predicted by AQZ-CCSD(T) levels are

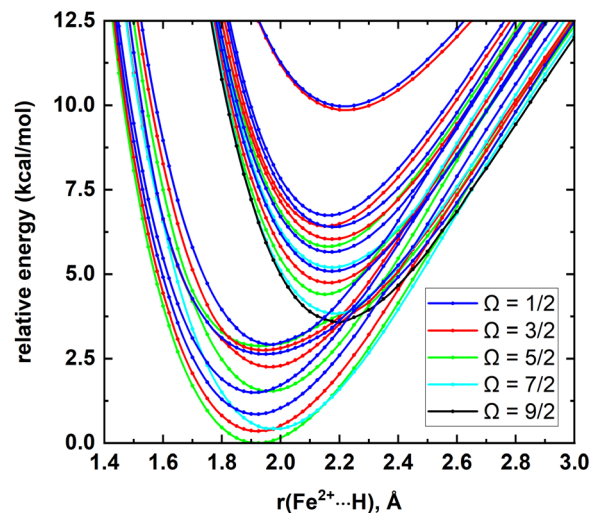


Fig. 5 AQZ-DK-MRCI spin-orbit coupling curves resulting from  $^4\Pi$ ,  $^4\Delta$ ,  $^6\Sigma^+$ ,  $^6\Delta$ ,  $^6\Pi$ , and  $^4\Sigma^+$  electronic states of  $\text{FeH}^{2+}$  as a function of  $\text{Fe}^{2+}\cdots\text{H}$  distance [ $r(\text{Fe}^{2+}\cdots\text{H})$ , Å]. The relative energies are referenced with respect to the  $\Omega = 5/2$  ground state minimum of  $\text{FeH}^{2+}$ . The  $\Omega = 1/2$ ,  $\Omega = 3/2$ ,  $\Omega = 5/2$ ,  $\Omega = 7/2$ , and  $\Omega = 9/2$  curves are shown in blue, red, green, cyan, and black, respectively. See Fig. 4 for the PEC of their parent  $^4\Pi$ ,  $^4\Delta$ ,  $^6\Sigma^+$ ,  $^6\Delta$ ,  $^6\Pi$ , and  $^4\Sigma^+$  states.

Table 6 Bond length  $r_e$  (Å), excitation energy  $T_e$  (cm $^{-1}$ ), harmonic vibrational frequency  $\omega_e$  (cm $^{-1}$ ), and %  $\Lambda S$  composition of several low-lying spin-orbit states of  $\text{FeH}^{2+}$  at AQZ-DK-MRCI level

$\Omega$	$r_e$	$T_e$	$\omega_e$	$\Lambda S$ composition <sup>a</sup>
5/2	1.922	0	810	78% $^4\Pi$ + 20% $^4\Delta$ + 2% $^6\Sigma^+$
3/2	1.919	123	823	82% $^4\Pi$ + 16% $^4\Delta$ + 2% $^6\Sigma^+$
7/2	1.958	150	858	100% $^4\Delta$
1/2	1.917	299	808	88% $^4\Pi$ + 10% $^4\Delta$ + 2% $^6\Sigma^+$
1/2	1.909	524	867	98% $^4\Pi$ + 2% $^6\Sigma^+$
5/2	1.966	538	913	72% $^4\Delta$ + 25% $^4\Pi$ + 3% $^6\Sigma^+$
3/2	1.964	789	833	75% $^4\Delta$ + 17% $^4\Pi$ + 8% $^6\Sigma^+$
1/2	1.947	921	626	85% $^6\Sigma^+$ + 9% $^4\Delta$ + 5% $^6\Pi$
3/2	1.942	964	724	85% $^6\Sigma^+$ + 6% $^4\Pi$ + 5% $^6\Pi$ + 4% $^4\Delta$
5/2	1.929	1007	675	93% $^6\Sigma^+$ + 4% $^4\Pi$ + 2% $^6\Pi$
1/2	1.967	1021	862	79% $^4\Delta$ + 14% $^4\Pi$ + 6% $^6\Sigma^+$
9/2	2.197	1250	904	100% $^6\Delta$
7/2	2.187	1341	916	80% $^6\Delta$ + 20% $^6\Pi$
5/2	2.150	1539	1031	65% $^6\Delta$ + 23% $^6\Sigma^+$ + 10% $^6\Pi$ + 1% $^4\Pi$
3/2	2.164	1659	917	64% $^6\Delta$ + 23% $^6\Pi$ + 12% $^6\Sigma^+$ + 1% $^4\Pi$
1/2	2.173	1778	896	53% $^6\Delta$ + 42% $^6\Pi$ + 4% $^6\Sigma^+$ + 1% $^4\Pi$
7/2	2.174	1818	825	78% $^6\Pi$ + 21% $^6\Delta$ + 1% $^4\Delta$
1/2	2.169	1978	869	61% $^6\Delta$ + 30% $^6\Pi$ + 8% $^6\Sigma^+$ + 1% $^4\Pi$
5/2	2.161	2035	924	66% $^6\Pi$ + 23% $^6\Delta$ + 10% $^6\Sigma^+$ + 1% $^4\Delta$
3/2	2.174	2112	822	76% $^6\Pi$ + 22% $^6\Delta$
1/2	2.179	2238	743	53% $^6\Pi$ + 45% $^6\Delta$ + 2% $^6\Sigma^+$
3/2	2.153	2247	826	77% $^6\Pi$ + 15% $^6\Sigma^+$ + 8% $^6\Delta$
1/2	2.162	2358	830	57% $^6\Pi$ + 31% $^6\Delta$ + 11% $^6\Sigma^+$
3/2	2.220	3449	667	98% $^4\Sigma^+$ + 1% $^6\Pi$ + 1% $^4\Pi$
1/2	2.215	3487	732	97% $^4\Sigma^+$ + 3% $^4\Pi$

<sup>a</sup> Only components that are equal or larger than 1% are listed.

larger than the AQZ-MRCI  $\mu$ . The calculated AQZ-MRCI DMC of the 6 low-lying states of  $\text{FeH}^{2+}$  are shown in Fig. 6a. Similar to  $\text{FeH}^+$ , the  $\mu$  values of  $\text{FeH}^{2+}$  increase moving to shorter internuclear distances and shift towards the negative direction. The



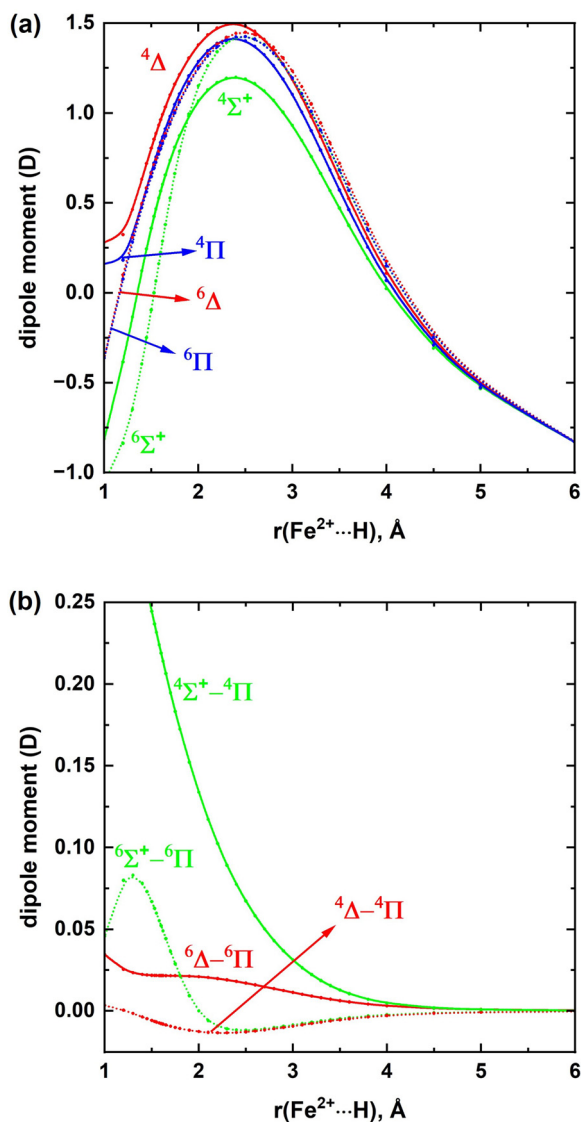


Fig. 6 (a) AQZ-MRCI DMC of  $\text{FeH}^{2+}$  as a function of  $\text{Fe}^{2+}\cdots\text{H}$  distance  $[r(\text{Fe}^{2+}\cdots\text{H}), \text{\AA}]$ . The solid and dotted DMC correspond to the quartet and sextet spins, respectively. The  $\Delta$ ,  $\Pi$ , and  $\Sigma^+$  states are shown in red, blue, and green, respectively. (b) AQZ-MRCI TDMC resulting from  $^4\Delta \leftrightarrow ^4\Pi$ ,  $^6\Delta \leftrightarrow ^6\Pi$ ,  $^6\Sigma^+ \leftrightarrow ^6\Pi$ , and  $^4\Sigma^+ \leftrightarrow ^4\Pi$  of  $\text{FeH}^{2+}$  as a function of  $\text{Fe}^{2+}\cdots\text{H}$  distance  $[r(\text{Fe}^{2+}\cdots\text{H}), \text{\AA}]$ .

maxima of the DMC were observed around the 2.4–2.5 Å. Only  $^4\Delta \leftrightarrow ^4\Pi$ ,  $^6\Delta \leftrightarrow ^6\Pi$ ,  $^6\Sigma^+ \leftrightarrow ^6\Pi$ , and  $^4\Sigma^+ \leftrightarrow ^4\Pi$  transitions are allowed for the studied states of  $\text{FeH}^{2+}$ . The TDMC corresponding to these transitions are illustrated in the Fig. 6b. Among these transitions, the smallest transition  $\mu$  values were observed for the  $\Delta \leftrightarrow \Pi$ . Comparatively, the  $\Sigma^+ \leftrightarrow \Pi$  transition  $\mu$  values are significant. Especially, the  $^4\Sigma^+ \leftrightarrow ^4\Pi$  transition  $\mu$  values increase exponentially moving to shorter internuclear distances.

### III.C. TIPS of $\text{FeH}^+$ and $\text{FeH}^{2+}$

In the TIPS calculations of the of  $\text{FeH}^+$  and  $\text{FeH}^{2+}$ , we included all bound rovibrational levels<sup>50</sup> that were allowed from the respective PEC (see Fig. 1 and 4). Here the  $\text{FeH}^+$   $3^3\Sigma^-$ ,  $1^3\text{H}$ ,

and  $3^3\Delta$  PEC were extrapolated by fitting each PEC with an extended Morse PEC, noting that these states are products of the  $\text{Fe}^+(\text{a}^2\text{H}) + \text{H}(\text{S})$  reaction. For the states included within the  $\text{FeH}^+$  and  $\text{FeH}^{2+}$  models, we estimate that the present TIPS results are accurate (within  $\sim 0.05\%$ ) up to approximately 5000 K and 1000 K, respectively. However, the errors associated with the accuracy of the PEC and solution of the rovibrational Schrödinger equation are not taken into account. We expect that the present TIPS calculation will have reasonable errors at low temperatures  $\lesssim 1500$  K, where the accuracy of the method, spin–orbit coupling and non-adiabatic effects can be relatively important to the TIPS. This is the first presentation of the  $\text{FeH}^+$  and  $\text{FeH}^{2+}$  TIPS in the literature, hence we provide results for the TIPS beyond the expected range of accuracy.

The following TIPS fit function<sup>62</sup>

$$\log_{10}(Q) = \sum_{n=1}^{N-1} a_n \left[ \log_{10} \left( \frac{5040 \text{ K}}{T + a_0} \right) \right]^{n-1},$$

can represent the TIPS over the temperature range 10–30 000 K (and perhaps even over a broader range). The  $a$  coefficients were optimized to minimize the maximum error of the fit function, noting that we fit the TIPS over a broader range of temperatures than we expect the TIPS to be accurate for in equations of state calculations. The  $\text{FeH}^+$  and  $\text{FeH}^{2+}$   $N = 17$  and  $N = 19$  fit coefficients are given in ESI,<sup>†</sup> Tables S2 and S3, where the errors of the fit functions are less than approximately 0.06% and 0.07%, respectively over the 10–30 000 K range. Note this error is only due to the fit (see above).

## IV. Conclusions

The MRCI and CCSD(T) WFT calculations were performed with large correlation consistent basis sets to analyze the ground and excited electronic states of  $\text{FeH}^+$  and  $\text{FeH}^{2+}$ . Multireference calculations were constructed using a bigger active space made of the five 3d, five 4d, and the 4s atomic orbitals of Fe and the 1s atomic orbital of H. We introduced 27 and 6 MRCI PEC for  $\text{FeH}^+$  and  $\text{FeH}^{2+}$ , respectively. The  $\omega_e$ ,  $\omega_e x_e$ ,  $B_e$ ,  $\alpha_e$ ,  $\bar{D}_e$  spectroscopic parameters and  $r_e$ ,  $T_e$ , and  $\mu$  values of  $\text{FeH}^+$  and  $\text{FeH}^{2+}$  were obtained using the CCSD(T), MRCI, and MRCI+Q levels of theory. At the MRCI level, spin–orbit coupling effect of  $\text{FeH}^+$  and  $\text{FeH}^{2+}$  were also tested.  $\text{FeH}^+$  has 10 bound electronic states with respect to the  $\text{Fe}^+(\text{D}) + \text{H}(\text{S})$  fragments, but 3 of them are relatively weakly bound with less than 3 kcal mol<sup>−1</sup>  $D_e$ . The ground state of  $\text{FeH}^+$  is a  $\text{X}^5\Delta$  with a  $D_0$  51.8 kcal mol<sup>−1</sup>. This value is in reasonable agreement with the previously reported experimental  $D_0$  value of  $\text{FeH}^+$  (i.e.,  $48.9 \pm 1.4$  kcal mol<sup>−1</sup>). The  $\text{FeH}^+(\text{X}^5\Delta)$  bears the  $6\sigma^2 7\sigma^1 3\pi^2 1\delta^3$  electronic configuration which can be produced by ionizing an electron from the  $7\sigma^2$  of the dominant configuration of the  $\text{FeH}(\text{X}^4\Delta)$ . The calculated IE of this process is 7.425 eV. Among the studied electronic states, the largest  $\mu$  was observed for the ground state of  $\text{FeH}^+(\text{X}^5\Delta)$ . For all states we observed a good agreement between AQZ-MRCI  $\mu$  versus c-A5Z-CCSD(T)  $\mu$ . The  $\mu$  values of single-reference  $\text{FeH}^+(\text{X}^5\Delta)$  were calculated with a series of



functionals that span multiple rungs of Jacob's ladder of DFA and compared with the highly reliable CCSD(T) value obtained with the finite-field method. In agreement with our expectation, we observed a general trend of improving  $\mu$  going from lower to higher rungs of Jacob's ladder of DFA. Furthermore, we introduced the MRCI DMC and TDMC corresponding to several low-lying electronic states of  $\text{FeH}^+$  and  $\text{FeH}^{2+}$ . Compared to the  $\text{FeH}^+(X^5\Delta)$ , the  $\text{FeH}^{2+}(^4\Pi)$  is  $\sim 30$  kcal mol $^{-1}$  less strongly bound. The two most stable electronic states of  $\text{FeH}^{2+}$  (*i.e.*,  $^4\Pi$  and  $^4\Delta$ ) are multireference in nature and bound by  $\sim 23$  kcal mol $^{-1}$  with respect to  $\text{Fe}^{2+}(^5D) + \text{H}(^2S)$  dissociation. Lower  $\mu$  values were observed for the low-lying electronic states of  $\text{FeH}^{2+}$  compared to those of  $\text{FeH}^+$ . The transition  $\mu$  values for both  $\text{FeH}^+$  and  $\text{FeH}^{2+}$  are relatively small and hence we expect those transitions to produce weak bands in the corresponding spectra. Finally, we provided a fit function and coefficients for calculation of the  $\text{FeH}^+$  and  $\text{FeH}^{2+}$  TIPS. These are the only available TIPS data in the literature for these molecules.

## Data availability

The data supporting this article have been included as part of the ESI.†

## Conflicts of interest

There are no conflicts to declare.

## Acknowledgements

This work was supported by the National Aeronautics and Space Administration (NASA) ROSES-NRA NNH20ZDA001N-XRP, Los Alamos National Laboratory (LANL) Laboratory Directed Research and Development projects 20240039DR and 20240737PRD1. This research used resources provided by the Los Alamos National Laboratory Institutional Computing Program, which is supported by the U.S. Department of Energy National Nuclear Security Administration under Contract No. 89233218CNA000001. Reviewers are thanked for their useful comments on improving this work.

## References

- H. R. Johnson and A. J. Sauval, *A&AS*, 1982, **49**, 77–87.
- E. I. Mysov, I. R. Lyatifov, R. B. Materikova and N. S. Kochetkova, *J. Organomet. Chem.*, 1979, **169**, 301–308.
- L. F. Halle, F. S. Klein and J. L. Beauchamp, *J. Am. Chem. Soc.*, 1984, **106**, 2543–2549.
- J. B. Schilling, W. A. Goddard and J. L. Beauchamp, *J. Am. Chem. Soc.*, 1986, **108**, 582–584.
- J. L. Elkind and P. B. Armentrout, *J. Phys. Chem.*, 1986, **90**, 5736–5745.
- J. B. Schilling, W. A. Goddard and J. L. Beauchamp, *J. Phys. Chem.*, 1987, **91**, 5616–5623.
- L. G. M. Pettersson, C. W. Bauschlicher, S. R. Langhoff and H. Partridge, *J. Chem. Phys.*, 1987, **87**, 481–492.
- M. Sodupe, J. M. Lluch, A. Oliva, F. Illas and J. Rubio, *J. Chem. Phys.*, 1989, **90**, 6436–6442.
- S. R. Langhoff and C. W. Bauschlicher, Jr., *Astrophys. J.*, 1991, **375**, 843–845.
- Q. Cheng and N. J. DeYonker, *J. Chem. Phys.*, 2019, **150**, 234304.
- S. Jin, J. Heller, C. van der Linde, M. Oncak and M. K. Beyer, *J. Phys. Chem. Lett.*, 2022, **13**, 5867–5872.
- D. J. D. Wilson, C. J. Marsden and E. I. von Nagy-Felsobuki, *Phys. Chem. Chem. Phys.*, 2003, **5**, 252–258.
- H.-J. Werner and P. J. Knowles, *J. Chem. Phys.*, 1988, **89**, 5803–5814.
- P. J. Knowles and H.-J. Werner, *Chem. Phys. Lett.*, 1988, **145**, 514–522.
- K. R. Shamasundar, G. Knizia and H. J. Werner, *J. Chem. Phys.*, 2011, **135**, 054101.
- S. R. Langhoff and E. R. Davidson, *Int. J. Quantum Chem.*, 1974, **8**, 61–72.
- K. Raghavachari, G. W. Trucks, J. A. Pople and M. Head-Gordon, *Chem. Phys. Lett.*, 1989, **157**, 479–483.
- J. P. Perdew and K. Schmidt, *AIP Conf. Proc.*, 2001, **577**, 1–20.
- H. J. Werner, P. J. Knowles, G. Knizia, F. R. Manby and M. Schütz, *Wiley Interdiscip. Rev.: Comput. Mol. Sci.*, 2011, **2**, 242–253.
- H. J. Werner, P. J. Knowles, F. R. Manby, J. A. Black, K. Doll, A. Hesselmann, D. Kats, A. Kohn, T. Korona, D. A. Kreplin, Q. Ma, T. F. Miller, 3rd, A. Mitrushchenkov, K. A. Peterson, I. Polyak, G. Rauhut and M. Sibaev, *J. Chem. Phys.*, 2020, **152**, 144107.
- H.-J. Werner, P. J. Knowles, *et al.*, *MOLPRO, version 2023.2, a package of ab initio programs*, see <https://www.molpro.net>.
- N. B. Balabanov and K. A. Peterson, *J. Chem. Phys.*, 2005, **123**, 64107.
- R. A. Kendall, T. H. Dunning and R. J. Harrison, *J. Chem. Phys.*, 1992, **96**, 6796–6806.
- H.-J. Werner and P. J. Knowles, *J. Chem. Phys.*, 1985, **82**, 5053–5063.
- P. J. Knowles and H.-J. Werner, *Chem. Phys. Lett.*, 1985, **115**, 259–267.
- D. A. Kreplin, P. J. Knowles and H. J. Werner, *J. Chem. Phys.*, 2019, **150**, 194106.
- D. A. Kreplin, P. J. Knowles and H. J. Werner, *J. Chem. Phys.*, 2020, **152**, 074102.
- I. R. Ariyaratna, J. A. Leiding, A. J. Neukirch and M. C. Zammit, *J. Phys. Chem. A*, 2024, **128**, 9412–9425.
- J. P. Perdew, *Phys. Rev. B: Condens. Matter Mater. Phys.*, 1986, **33**, 8822–8824.
- A. D. Becke, *Phys. Rev. A*, 1988, **38**, 3098–3100.
- B. Miehlich, A. Savin, H. Stoll and H. Preuss, *Chem. Phys. Lett.*, 1989, **157**, 200–206.
- F. J. Devlin, J. W. Finley, P. J. Stephens and M. J. Frisch, *J. Phys. Chem.*, 1995, **99**, 16883–16902.
- J. P. Perdew, K. Burke and M. Ernzerhof, *Phys. Rev. Lett.*, 1996, **77**, 3865–3868.





- 34 J. Tao, J. P. Perdew, V. N. Staroverov and G. E. Scuseria, *Phys. Rev. Lett.*, 2003, **91**, 146401.
- 35 H. S. Yu, X. He and D. G. Truhlar, *J. Chem. Theory Comput.*, 2016, **12**, 1280–1293.
- 36 A. D. Becke, *J. Chem. Phys.*, 1993, **98**, 5648–5652.
- 37 C. Lee, W. Yang and R. G. Parr, *Phys. Rev. B: Condens. Matter Mater. Phys.*, 1988, **37**, 785–789.
- 38 P. J. Stephens, F. J. Devlin, C. F. Chabalowski and M. J. Frisch, *J. Phys. Chem.*, 1994, **98**, 11623–11627.
- 39 J. P. Perdew, J. A. Chevary, S. H. Vosko, K. A. Jackson, M. R. Pederson, D. J. Singh and C. Fiolhais, *Phys. Rev. B: Condens. Matter Mater. Phys.*, 1992, **46**, 6671–6687.
- 40 C. Adamo and V. Barone, *J. Chem. Phys.*, 1999, **110**, 6158–6170.
- 41 Y. Zhao and D. G. Truhlar, *Theor. Chem. Acc.*, 2007, **120**, 215–241.
- 42 H. S. Yu, X. He, S. L. Li and D. G. Truhlar, *Chem. Sci.*, 2016, **7**, 5032–5051.
- 43 M. A. Rohrdanz, K. M. Martins and J. M. Herbert, *J. Chem. Phys.*, 2009, **130**, 054112.
- 44 T. Yanai, D. P. Tew and N. C. Handy, *Chem. Phys. Lett.*, 2004, **393**, 51–57.
- 45 J. D. Chai and M. Head-Gordon, *J. Chem. Phys.*, 2008, **128**, 084106.
- 46 E. Bremond and C. Adamo, *J. Chem. Phys.*, 2011, **135**, 024106.
- 47 S. Kozuch and J. M. Martin, *Phys. Chem. Chem. Phys.*, 2011, **13**, 20104–20107.
- 48 S. Kozuch and J. M. Martin, *J. Comput. Chem.*, 2013, **34**, 2327–2344.
- 49 M. J. Frisch, G. W. Trucks, H. B. Schlegel, G. E. Scuseria, M. A. Robb, J. R. Cheeseman, G. Scalmani, V. Barone, G. A. Petersson, H. Nakatsuji, X. Li, M. Caricato, A. V. Marenich, J. Bloino, B. G. Janesko, R. Gomperts, B. Mennucci, H. P. Hratchian, J. V. Ortiz, A. F. Izmaylov, J. L. Sonnenberg, D. Williams, F. Ding, F. Lipparini, F. Egidi, J. Goings, B. Peng, A. Petrone, T. Henderson, D. Ranasinghe, V. G. Zakrzewski, J. Gao, N. Rega, G. Zheng, W. Liang, M. Hada, M. Ehara, K. Toyota, R. Fukuda, J. Hasegawa, M. Ishida, T. Nakajima, Y. Honda, O. Kitao, H. Nakai, T. Vreven, K. Throssell, J. A. Montgomery Jr., J. E. Peralta, F. Ogliaro, M. J. Bearpark, J. J. Heyd, E. N. Brothers, K. N. Kudin, V. N. Staroverov, T. A. Keith, R. Kobayashi, J. Normand, K. Raghavachari, A. P. Rendell, J. C. Burant, S. S. Iyengar, J. Tomasi, M. Cossi, J. M. Millam, M. Klene, C. Adamo, R. Cammi, J. W. Ochterski, R. L. Martin, K. Morokuma, O. Farkas, J. B. Foresman and D. J. Fox, *Gaussian 16*, Gaussian Inc., Wallingford CT, 2016.
- 50 M. C. Zammit, J. A. Leiding, J. Colgan, W. Even, C. J. Fontes and E. Timmermans, *J. Phys. B: At., Mol. Opt. Phys.*, 2022, **55**, 184002.
- 51 J. K. Kirkland, S. N. Khan, B. Casale, E. Miliordos and K. D. Vogiatzis, *Phys. Chem. Chem. Phys.*, 2018, **20**, 28786–28795.
- 52 N. M. S. Almeida, I. R. Ariyaratna and E. Miliordos, *J. Phys. Chem. A*, 2019, **123**, 9336–9344.
- 53 A. Kramida, Y. Ralchenko and J. Reader, *NIST Atomic Spectra Database (Version 5.3)*, National Institute of Standards and Technology, Gaithersburg, MD, 2015, <https://physics.nist.gov/asd>.
- 54 R. S. Mulliken, *Rev. Mod. Phys.*, 1932, **4**, 1–86.
- 55 E. Wigner and E. E. Witmer, *Z. Phys.*, 1928, **51**, 859–886.
- 56 K. K. Irikura, W. A. Goddard and J. L. Beauchamp, *Int. J. Mass Spectrom. Ion Processes*, 1990, **99**, 213–222.
- 57 I. R. Ariyaratna and E. Miliordos, *Phys. Chem. Chem. Phys.*, 2018, **20**, 12278–12287.
- 58 I. R. Ariyaratna, C. Duan and H. J. Kulik, *J. Chem. Phys.*, 2022, **156**, 184113.
- 59 I. R. Ariyaratna and E. Miliordos, *J. Quant. Spectrosc. Radiat. Transfer*, 2020, **255**, 107265.
- 60 I. R. Ariyaratna, *Phys. Chem. Chem. Phys.*, 2024, **26**, 21099–21109.
- 61 I. R. Ariyaratna, *Phys. Chem. Chem. Phys.*, 2024, **26**, 22858–22869.
- 62 A. J. Sauval and J. B. Tatum, *Astrophys. J., Suppl. Ser.*, 1984, **56**, 193–209.

